

Digital quantum simulation of scalar Yukawa coupling

Thierry N. Kaldenbach^{a,b}, Matthias Heller^{*b,c}, Gernot Alber^a, and
Vladimir M. Stojanović^{†a}

^aInstitut für Angewandte Physik, Technical University of
Darmstadt, D-64289 Darmstadt, Germany

^bFraunhofer-Institut für Graphische Datenverarbeitung IGD,
D-64283 Darmstadt, Germany

^cTechnical University of Darmstadt, Karolinenplatz 5, D-64289
Darmstadt, Germany

Abstract

Motivated by the revitalized interest in the digital quantum simulation of coupled fermion-boson models from medium- and high-energy physics, we investigate the nonequilibrium dynamics following a Yukawa-interaction quench on IBM Q. Adopting – due to current quantum-hardware limitations – a single-site (zero-dimensional) version of the scalar Yukawa-coupling model as our point of departure, we design low-depth quantum circuits that emulate its dynamics with up to three bosons. In particular, using advanced circuit-optimization techniques, in the one-boson case we demonstrate circuit compression, i.e. design a constant-depth circuit containing only two CNOT gates, regardless of the total simulation time. In the three-boson case – where such a compression is not possible – we design a circuit in which one Trotter step entails 8 CNOTs, this number being far below the maximal CNOT-cost of a generic three-qubit gate. Using an analogy with the travelling salesman problem, we also provide a CNOT-cost estimate for quantum circuits emulating the system dynamics for higher boson-number truncations. Based on the designed circuits, we quantify the system dynamics for the initial vacuum state by evaluating the expected boson number at an arbitrary time after a Yukawa-interaction quench, as well as the survival probability of the initial state (the Loschmidt echo). Finally, we make use of the designed circuits to drive adiabatic transitions and compute the energies of the ground- and first excited state of the model under consideration. We validate our results by performing error mitigation in the form of zero-noise extrapolation, finding an excellent agreement of our obtained results with the exact ones obtained through classical benchmarking.

*matthias.heller@igd.fraunhofer.de

†vladimir.stojanovic@physik.tu-darmstadt.de

1 Introduction

The reinvigorated research interest in *digital quantum simulation* (DQS) [1–3] has chiefly been motivated by the tantalizing recent progress in the development and deployment of quantum hardware based on superconducting- [4], trapped-ion- [5], or neutral-atom systems [6]. This recent flurry of research activity in DQS was preceded by a large body of investigation pertaining to analog quantum simulators [3] of many-body systems that had been accrued over the period of nearly two decades. Both of these research strands have in large part been inspired by the pioneering assertion of Feynman that a generic quantum system could efficiently be simulated using a device whose operation is also governed by quantum-mechanical laws [7]. Admittedly, the field of DQS has heretofore been dominated by the development and application of quantum algorithms for simulating purely fermionic systems [8–18]; this is mostly related to the fact that – owing to the existence of the Pauli exclusion principle – simulations of such systems typically require relatively modest quantum-hardware resources.

Unlike their fermionic counterparts, quantum many-body systems involving bosonic constituents have infinite-dimensional Hilbert spaces that ought to be truncated if one aims to simulate such systems on either classical or quantum computers. Due to the inherently nontrivial problem of encoding bosonic states on qubit registers, the DQS of bosonic systems has heretofore received comparatively modest attention [19–22]. In particular, while many analog simulators of *coupled fermion-boson* models [19, 23] have been proposed [24–30], only a handful of such models have as yet been addressed in the DQS context [20, 31]. Motivated by the dearth of research activity pertaining to the DQS of coupled fermion-boson models, as well as the emerging trend of simulating models from medium- and high-energy physics [31–37], in this paper we present a DQS of the nonequilibrium dynamics following a quench [38] of the scalar Yukawa interaction [39]. Such coupling – first proposed for describing the nucleon-nucleon interaction mediated by pions [40] – involves fermion-, antifermion-, and boson degrees of freedom. Due to limitations of current noisy intermediate-scale quantum hardware [41], here we investigate the low-energy limit of the scalar Yukawa coupling on a single lattice site, with low truncation numbers for the real scalar (boson) field. We show that, despite its inherent simplicity, the resulting zero-dimensional model shows nontrivial quantum dynamics.

By first making use of the local charge conservation in the system at hand, which allows us to encode the fermion-antifermion sector of the problem using a single qubit, we subsequently design low-depth quantum circuits that emulate the system dynamics with up to three bosons. We then implement those circuits on state-of-the-art IBM Quantum (IBM Q) hardware [42], based on quantum processors that rely on the use of controlled-NOT (CNOT) as a representative two-qubit gate. Based on the designed circuits, we characterize the system dynamics for the vacuum state by computing the expected boson numbers and the survival probability of the initial state (the Loschmidt echo) [43] at an arbitrary time after the quench. We then use similar techniques to construct circuits to calculate the energies of the ground state and first excited state using adiabatic state preparation [44, 45] on IBM Q. We also provide a benchmark for the obtained results by carrying out a numerically-exact evaluation of the aforementioned quantities on a classical computer.

Using sophisticated circuit-optimization techniques, in the one-boson case –

which in our realization corresponds to a two-qubit system – we demonstrate circuit compression. More precisely, we design a constant-depth circuit that contains only two CNOT gates, regardless of the total simulation time. In other words, in this case we find a much more efficient realization than the conventional one in which the circuit depth scales linearly with the number of Trotter steps. Such circuit compressions are only possible for certain special types of the system (coupled-qubit) Hamiltonian and have quite recently been discussed in the context of the transverse-field Ising- [46,47] and XY [29] models by means of Lie-algebraic methods [48], as well as using reflection symmetry and the quantum Yang-Baxter equation [49]. The shallow circuits resulting from such compressions have depths that are completely independent of the Trotter-step size and depend only on the number of qubits.

On the other hand, in the more nontrivial three-boson case – which in our adopted state-encoding scheme corresponds to a three-qubit system – a compression to a constant-depth circuit is no longer possible. We show that in this case it proves beneficial to make use of the second-order Trotter-Suzuki product formula [50,51], which entails a symmetrized Trotter step. Using this symmetrized Trotter decomposition, we design a circuit in which one Trotter step entails 8 CNOTs. This last number of CNOTs is far below the maximal CNOT-cost (14) of a generic three-qubit gate [52], which speaks in favor of the efficiency of the proposed circuit [52,53].

We also address cases with larger boson-number truncations by providing the CNOT-cost estimate for quantum circuits that emulate the system dynamics in those cases. We do so based on an analogy of our circuit optimization with the *travelling salesman problem* (TSP) [54], adapting an idea proposed in Ref. [77]. To this end, we make use of the exact solution of the TSP based on the Bellman-Held-Karp dynamic-programming algorithm [55,56] – which due to its unfavorable time-complexity is limited to rather low truncations – as well as the Christofides algorithm, a polynomial-time heuristic that approximately solves the TSP on a metric graph [57]. Being polynomial in character, the latter can be utilized for much larger boson-number truncations.

While the simplified, zero-dimensional version of the scalar Yukawa-coupling model cannot be expected to bear out all the relevant features of the actual physical phenomenon, our primary aim here is to use the DQS of this simple model as a testbed for IBM Q hardware. In particular, we perform error-mitigation in the form of *zero-noise extrapolation* [82,83], having previously verified that the physical noise in the quantum processor used can be described using the depolarizing-noise channel model [64]. This widely used error-mitigation technique allows us to obtain results that are in excellent agreement with the numerically-exact classical benchmark. Moreover, we find that some approaches to the zero-noise extrapolation (circuit folding) work better here than the other ones (gate folding), a useful insight about the behaviour of the IBM Q processors under error mitigation of this type.

The remainder of this paper is organized as follows. In Sec. 2 we introduce the fermion-boson system under consideration and its underlying Hamiltonian. Section 3 starts with a short description of our scheme for describing the system dynamics after an interaction quench via DQS, followed by a brief recapitulation of our adopted approaches for encoding the relevant fermion- and boson states on dedicated registers of qubits. At the end of this section, we also address the issue of the controllable truncation of the bosonic Hilbert space. Section 4

starts with the design of low-depth quantum circuits emulating the dynamics of the system, first in the two-qubit- and then in the three-qubit case. This is followed by an analysis of the CNOT-cost for higher boson-number truncations. Finally, this section ends with a brief review of the basic aspects of the zero-noise extrapolation technique of error mitigation. The principal results obtained for the system dynamics on IBM Q, along with their comparison with the exact ones obtained through classical benchmarking, are presented in Sec. 5. We summarize the main findings of the paper and conclude in Sec. 6. Some cumbersome derivations, as well as certain relevant mathematical and computational details, are relegated to Appendices A - F.

2 System and Hamiltonian

To set the stage for further considerations, we first introduce the system at hand and its underlying fermion-boson Hamiltonian. We start by introducing the scalar Yukawa-coupling model (Sec. 2.1), and then specialize to its single-site (zero-dimensional) version (Sec. 2.2).

2.1 Scalar Yukawa coupling

The Yukawa-interaction mechanism was originally introduced to describe the nuclear force between nucleons mediated by pions [40]. It later attracted interest in the context of the Standard Model of particle physics, where it describes the coupling between the Higgs field and massless quark and lepton fields (i.e. the fundamental fermion fields); the latter fermion fields acquire masses, via the Higgs mechanism, after electroweak symmetry breaking [39]. Finally, it is worthwhile mentioning that interaction mechanism somewhat analogous to Yukawa coupling are of relevance in the context of strongly-correlated systems in condensed-matter physics [59].

In the following, we will be interested in the Yukawa-type interaction of a real scalar field ϕ and a Dirac field ψ , described by the Hamiltonian [39]

$$H_{\text{int}} = g \int d^3\mathbf{x} \, \bar{\psi}\psi\phi, \quad (1)$$

where g is the dimensionless coupling strength. While pions, which mediate the nucleon-nucleon interaction, are pseudoscalar mesons, we will assume a scalar interaction for the sake of simplicity. In our subsequent discussion, we adopt natural units, where $\hbar = c = 1$.

To perform a DQS of the real-time dynamics of scalar Yukawa coupling, we have to discretize the theory and select a convenient basis. While approaches that are directly based on the algebraic properties of the field operators do exist, in what follows we make use of an expansion in terms of creation and annihilation operators. We further select the momentum eigenstates $|\mathbf{p}\rangle$ as our preferred basis since it diagonalizes the free Hamiltonian. Using the definition of the Fourier transform $\phi(\mathbf{x}) = (2\pi)^{-3} \int d^3\mathbf{p} \, e^{i\mathbf{p}\cdot\mathbf{x}}\phi(\mathbf{p})$, one may rewrite the interaction Hamiltonian as

$$H_{\text{int}} = \frac{g}{2} \int \frac{d^3\mathbf{p}}{(2\pi)^3} \int \frac{d^3\mathbf{p}'}{(2\pi)^3} [\bar{\psi}(\mathbf{p})\psi(\mathbf{p}')\phi(\mathbf{p} - \mathbf{p}') + \text{H.c.}], \quad (2)$$

with the field operators in momentum space being defined as [39]

$$\begin{aligned}\phi(\mathbf{p}) &= \frac{1}{\sqrt{2\omega_{\mathbf{p}}}} \left(b_{\mathbf{p}} + b_{-\mathbf{p}}^{\dagger} \right), \\ \psi(\mathbf{p}) &= \frac{1}{\sqrt{2\Omega_{\mathbf{p}}}} \sum_s \left[a_{\mathbf{p}}^s u^s(\mathbf{p}) + c_{-\mathbf{p}}^{s\dagger} v^s(-\mathbf{p}) \right],\end{aligned}\tag{3}$$

with the relativistic dispersion relations $\omega_{\mathbf{p}}^2 = m^2 + \mathbf{p}^2$ (for bosons) and $\Omega_{\mathbf{p}}^2 = M^2 + \mathbf{p}^2$ (for fermions) [39]. By discretizing the integrals in Eq. (2) and using Eq. (3), one obtains the momentum-space version of H_{int} in terms of creation/annihilation operators

$$\begin{aligned}H_{\text{int}} &= \frac{ga_l^{3/2}}{2} \sum_{\mathbf{p}, \mathbf{p}'} \sum_{r,s} \left\{ \frac{1}{\sqrt{8\Omega_{\mathbf{p}}\Omega_{\mathbf{p}'}\omega_{\mathbf{p}-\mathbf{p}'}}} \left(b_{\mathbf{p}-\mathbf{p}'} + b_{\mathbf{p}'}^{\dagger} \right) \right. \\ &\times \left[a_{\mathbf{p}}^{r\dagger} \bar{u}^r(\mathbf{p}) + c_{-\mathbf{p}}^r \bar{v}^r(-\mathbf{p}) \right] \\ &\times \left[a_{\mathbf{p}'}^s u^s(\mathbf{p}') + c_{-\mathbf{p}'}^{s\dagger} v^s(-\mathbf{p}') \right] + \text{H.c.} \left. \right\},\end{aligned}\tag{4}$$

where a_l is the lattice spacing.

2.2 Single-site model

Due to technological limitations of current quantum hardware, it appears prudent to start investigating scalar Yukawa interaction on a single lattice site with low truncation numbers for the real scalar. While for large lattices the gate cost of the time evolution scales more favourably in real space, the momentum-space representation is still suitable for small lattices – especially in the extreme case of a single-site model. The single grid point in momentum space corresponds to a momentum below a certain small cutoff value for all particles, implying that all particles can be considered to be approximately at rest. While zero-dimensional, single-site models of this type are widely used in the context of the DQS of high/medium energy models [61, 62], it is obvious that they cannot be expected to yield accurate results for any relevant physical observable. However, such “toy models” can still display nontrivial quantum dynamics and can thus be seen as a useful first step towards more complex simulations that should be achievable in the not-too-distant future.

As derived in Appendix A, the effective interaction Hamiltonian of our single-site model is given by

$$H_{\text{int}} = \frac{\eta}{2} (a^{\dagger}a + c^{\dagger}c - 1) (b + b^{\dagger}),\tag{5}$$

with $\eta \equiv 4mg\beta^{3/2}$ being the effective coupling strength. At the same time, the single-site version of the free Hamiltonian $H_0 = H_{\text{Dirac}} + H_{\text{Klein-Gordon}}$ is given by

$$H_0 = M(a^{\dagger}a + c^{\dagger}c) + mb^{\dagger}b.\tag{6}$$

The sum of the Hamiltonians in Eqs. (5) and (6) – i.e. the Hamiltonian $H_{\text{tot}} = H_0 + H_{\text{int}}$ – will be our point of departure for simulating the dynamics following a quench of the scalar Yukawa coupling in what follows.

3 DQS of Hamiltonian dynamics and encoding fermion/boson states on qubits

To facilitate the discussion of the DQS of the Yukawa-coupled system in the remainder of this paper, we begin with some general considerations of the DQS of the dynamics following an interaction quench and quantum-circuit synthesis (Sec. 3.1). We then recapitulate the basic aspects of encoding the relevant particle states on qubits, both for fermions (Sec. 3.2) and bosons (Sec. 3.3). Finally, we discuss the truncation of the boson Hilbert space (Sec. 3.4).

3.1 Simulating the dynamics after an interaction quench

For a generic quantum system, described by a Hamiltonian H_{sys} , the Loschmidt amplitude [38]

$$\mathcal{G}(t) = \langle \psi_{t=0} | e^{-iH_{\text{sys}}t} | \psi_{t=0} \rangle \quad (7)$$

quantifies the deviation of the time-evolved state $|\psi_t\rangle \equiv e^{-iH_{\text{sys}}t} |\psi_{t=0}\rangle$ from the initial state $|\psi_{t=0}\rangle$. The Loschmidt echo [43] $\mathcal{L}(t) \equiv |\mathcal{G}(t)|^2$, the survival probability at time t of this initial state, represents the most widely used quantity in describing dynamics following an interaction quench. In order to evaluate this last quantity, as well as the expected boson number, at time t after a Yukawa-interaction quench, we will first evaluate the time-evolution operator of the system $U(t) \equiv e^{-iH_{\text{tot}}t}$ by representing it in the form of a quantum circuit, i.e. as a sequence of single- and two-qubit gates.

The unitary time-evolution operator $U(t)$ corresponding to the Hamiltonian $H(t)$ satisfies the time-dependent Schrödinger equation in the operator form $\partial U / \partial t = -iH(t)U(t)$, with the initial condition $U(t=0) = \mathbb{1}$. We will hereafter adopt a time-independent Hamiltonian $H(t) = H_{\text{sys}}$. By discretizing time into n steps of duration Δt , such that $t \equiv n\Delta t$ is the total evolution time, the time-evolution operator can be expressed as

$$U(t) = (e^{-iH_{\text{sys}}\Delta t})^n. \quad (8)$$

The inherent tradeoff pertaining to such a decomposition is that a smaller time step corresponds to a longer circuit. The last expression for $U(t)$ is typically approximated using first-order Trotter-Suzuki-type decomposition [50, 63]. For a time-independent Hamiltonian $H_{\text{sys}} = \sum_l H_l$ the latter approximates $\exp(-iH_{\text{sys}}t)$ by $(\prod_l e^{-iH_l t/n})^n$, with the corresponding error being upper bounded by $\mathcal{O}(Nt^2/n)$, where N is the number of qubits [1].

In the DQS context, time-evolution operators are represented through quantum circuits that emulate the system dynamics and are decomposed into single-qubit and two-qubit gates. Typical single-qubit gates include the Pauli gates [64]

$$X = \begin{bmatrix} 0 & 1 \\ 1 & 0 \end{bmatrix}, Y = \begin{bmatrix} 0 & -i \\ i & 0 \end{bmatrix}, Z = \begin{bmatrix} 1 & 0 \\ 0 & -1 \end{bmatrix}, \quad (9)$$

the single-qubit rotation gates

$$R_x(\theta) = e^{-\frac{i}{2}\theta X}, R_y(\theta) = e^{-\frac{i}{2}\theta Y}, R_z(\theta) = e^{-\frac{i}{2}\theta Z}, \quad (10)$$

as well as the Hadamard- (H), phase- (S) and $\pi/8$ (T) gates

$$H = \frac{1}{\sqrt{2}} \begin{bmatrix} 1 & 1 \\ 1 & -1 \end{bmatrix}, S = \begin{bmatrix} 1 & 0 \\ 0 & i \end{bmatrix}, T = \begin{bmatrix} 1 & 0 \\ 0 & e^{i\pi/4} \end{bmatrix}. \quad (11)$$

The essential two-qubit gate is controlled-NOT (CNOT), whose matrix representation is

$$\text{CNOT} = \begin{bmatrix} 1 & 0 & 0 & 0 \\ 0 & 1 & 0 & 0 \\ 0 & 0 & 0 & 1 \\ 0 & 0 & 1 & 0 \end{bmatrix}. \quad (12)$$

Simulating the dynamics of a quantum many-body system on a classical computer is typically a nontrivial problem due to the large Hilbert-space size that necessitates the allotment of a large amount of memory. The task of designing a circuit that emulates these same dynamics on a quantum computer [64] – a process often referred to as unitary synthesis – is exponentially hard. This is intimately related to exponential growth of a generic Hilbert space with the system size; for instance, for interacting fermion systems it is known that generating such a circuit is an NP-hard problem. What further complicates the already challenging task of unitary synthesis is the fact that near-term quantum hardware is both very limited in size and inevitably noisy [41]. Thus, the optimization of the quantum circuit emulating the dynamics of a relevant quantum system – i.e. reducing its depth in order to obtain as shallow a circuit as possible – is a task of paramount importance for DQS.

3.2 Fermion-state encoding

In the familiar Jordan-Wigner (JW) encoding [65] of fermion states, due to the Pauli exclusion principle, the fermionic occupation numbers are restricted to the set $\{0, 1\}$. This allows for a one-to-one mapping from the occupation-number basis to the computational basis. In other words, a qubit in the state $|0\rangle(|1\rangle)$ corresponds to an empty (occupied) fermionic orbital

$$|f_{n-1} \dots f_1 f_0\rangle \rightarrow |q_{n-1}\rangle \otimes \dots \otimes |q_1\rangle \otimes |q_0\rangle, \quad (13)$$

where f_j is the occupation number of orbital j ($j = 0, \dots, n-1$) and $|q_j\rangle$ the corresponding qubit state [$f_j = q_j \in \{0, 1\}$]. It should be emphasized that in writing Eq. (13) we assumed that the rightmost single-qubit state corresponds to the qubit 0, a convention that we will hereafter also utilize for operators.

The JW-type encoding requires $O(n)$ qubit operations to represent a fermionic operator, where n is the number of fermionic orbitals (or, in the problem at hand, momentum states of spin-up and spin-down particles/antiparticles). While the alternative, Bravyi-Kitaev encoding [10, 66] reduces this cost to $O(\log n)$, in what follows we will rely on the JW encoding as we will be concerned with Hamiltonians that are diagonal on the fermionic subspace in the occupation-number basis.

The JW qubit mappings of the fermion creation- and annihilation operators are, respectively, given by

$$\begin{aligned} c_j^\dagger &\equiv \frac{1}{2} (X_j - iY_j) \otimes Z_{j-1} \otimes \dots \otimes Z_1 \otimes Z_0, \\ c_j &\equiv \frac{1}{2} (X_j + iY_j) \otimes Z_{j-1} \otimes \dots \otimes Z_1 \otimes Z_0. \end{aligned} \quad (14)$$

Here the operators $(X_j \pm iY_j)/2$ change the occupation numbers of target spin orbital, while the action of the string of Z operators amounts to computing the parity of the state.

3.3 Boson-state encoding

Bosonic creation/annihilation operators satisfy the commutation relation $[b_i, b_j^\dagger] = \delta_{ij}$. In contrast to fermions, bosonic operators on different sites commute, thus they can be constructed such that they act locally on a bosonic mode. The main challenge in encoding bosonic states pertains to their unbounded occupation number, which forces us to impose an occupation-number cutoff Λ . The encoding of a bosonic Fock state with cutoff Λ requires $O(n \log \Lambda)$ qubits, where n is the number of bosonic modes. This scaling is achieved by representing the occupation numbers of the basis states of the truncated Fock space as binary strings and mapping the digits to single qubits [20]. For a Fock state $|k\rangle$, where k is an integer whose binary decomposition reads

$$k = \sum_{j=0}^{N-1} q_j(k) 2^j \quad (q_j \in \{0, 1\}), \quad (15)$$

the mapping is given by

$$|k\rangle \rightarrow |q_{N-1}\rangle \otimes \cdots \otimes |q_1\rangle \otimes |q_0\rangle. \quad (16)$$

The mapping of the truncated creation/annihilation operators to their pseudospin-1/2 (qubit) counterparts is then achieved by finding their corresponding Pauli-basis representations for arbitrary truncations. For a truncation at $\Lambda = 2^N - 1$, a bosonic creation operator can be represented as

$$b^\dagger = \left(\frac{1}{2}\right)^N \sum_{k=1}^{\Lambda} \sqrt{k} \bigotimes_{j=0}^{N-1} F_{j,k}, \quad (17)$$

where $F_{j,k}$ is an operator defined as (for a detailed derivation, see Appendix B)

$$F_{j,k} = \begin{cases} I_j + (-1)^{q_j(k)} Z_j & \text{if } \exists m < j : q_m(k) = 1 \\ X_j + (-1)^{q_j(k)} i Y_j & \text{if } \forall m < j : q_m(k) = 0 \end{cases}. \quad (18)$$

When taking the expectation value $\langle b^\dagger b \rangle$, we simply weight the probability that the k -th qubit is in state $|1\rangle$ by a factor of 2^k .

Another often used operator is the particle-number operator $b^\dagger b$, which in the Pauli basis is given by

$$b^\dagger b = \frac{1}{2} \sum_{j=0}^{N-1} 2^j (I - Z)_j. \quad (19)$$

3.4 Truncation of the boson Hilbert space

As discussed in Sec. 3.3, a truncation of the (infinite dimensional) boson Hilbert space is required in order to perform a DQS with a finite number of qubits. The ideal truncation depends non-trivially on the initial state of the system $|\psi_{t=0}\rangle$, the coupling strength η , and the total simulation time t . Throughout this work, we focus entirely on interaction quenches starting from the vacuum state as the initial state of the system. This obviates the need to consider the dependence of the system dynamics following a quench on the initial state. While theoretical

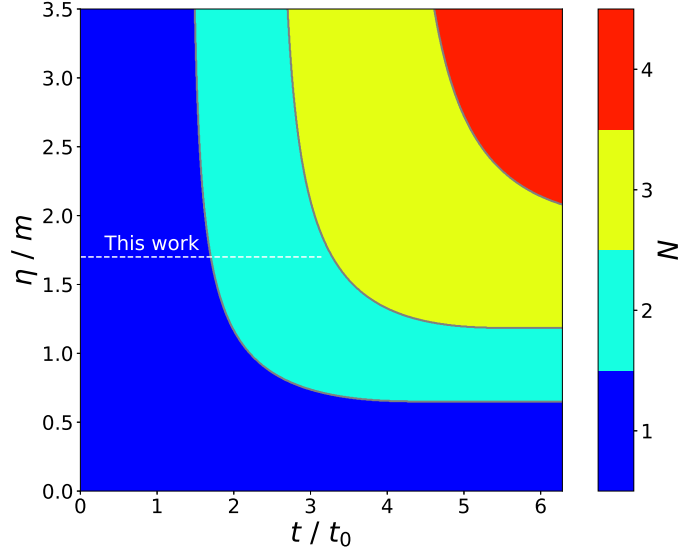


Figure 1: Qubit requirement N as a function of dimensionless time t/t_0 and the coupling-to-mass ratio η/m , where $t_0 \equiv 1/\sqrt{m^2 + \eta^2}$. To ensure that the target fidelity of 90% ($\epsilon = 0.1$) is attained, we can simulate the system using 2 bosonic qubits up to a time $t \approx 3t_0$.

estimations of the truncation required to keep the truncation error below a certain threshold are known [31], we will rely on classical simulations of our few-qubit quantum systems in order to determine the ideal qubit requirements. Our algorithm works as follows:

1. Define a high resolution grid of the coupling strength and the time in the regime of interest.
2. For each coupling strength, select an initial truncation with $N = 1$ qubits ($\Lambda = 1$).
3. Simulate the Hamiltonian with a truncation using N and $N + 1$ qubits on the time grid.
4. Compute the fidelity between both simulations for each point on the time grid. This is achieved by extending the lower dimensional state vector into the higher dimensional Hilbert space using the zero state $|\psi_N\rangle \rightarrow |0\rangle \otimes |\psi_N\rangle$.
5. If the fidelity falls below a certain threshold $1 - \epsilon$ at some point in time, the selected truncation is no longer appropriate. Then increase the qubit number by one ($N \rightarrow N + 1$), save the qubit number along with the time point, and repeat step 3, 4 and 5 until the desired fidelity is reached.

The results obtained using this algorithm are depicted in Figure 1. As can be inferred from that figure, using a coupling strength of $\eta = 1.7m$, we can simulate the dynamics of the system up to a time $t \approx 3t_0$, where $t_0 = 1/\sqrt{m^2 + \eta^2}$, with

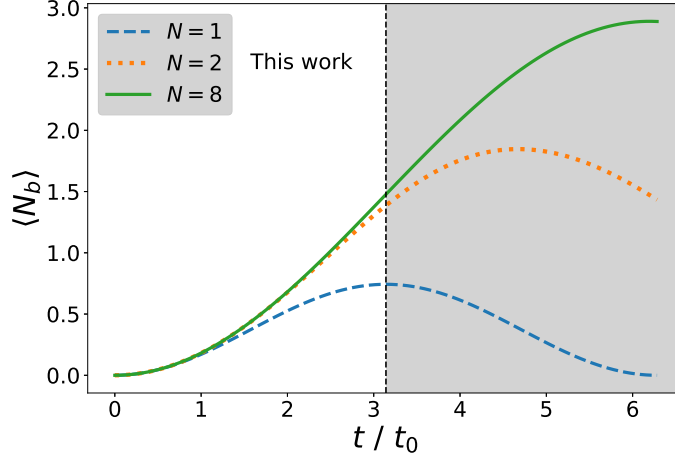


Figure 2: The bosonic occupation number $\langle N_b \rangle$ as a function of dimensionless time t/t_0 for a coupling-to-mass ratio of $\eta/m = 1.7$. Note, that the simulation with $N = 2$ shows good agreement with the $N = 8$ simulation up to a time $t \approx 3t_0$. The strong deviations on the right half indicate that a larger truncation is required for larger times, in agreement with the calculations from Fig. 1.

an accuracy of 90% using a boson truncation of $\Lambda = 3$ ($N = 2$). Bearing in mind the limited hardware resources of current quantum computers, we choose this system with a boson truncation of $\Lambda = 3$ (i.e. two bosonic qubits) as our reference system for DQS on an IBM quantum computer. This system shows non-trivial dynamics, and thus represents an ideal testbed for benchmarking quantum devices.

To examine how the truncation affects the dynamics of the system at hand, we perform classical simulations of the truncated system with $N = 1$, $N = 2$ and $N = 8$ (cf. Figure 2). Here, the truncation at the large value $N = 8$ is chosen in order to ensure that the system dynamics does not change upon further increase of N . As expected, we find a large deviation in the average boson number between the $N = 1$ (blue dashed curve) and $N = 2$ (orange dotted curve) in the relevant time interval, but a small deviation between the $N = 2$ and $N = 8$ case (green curve).

The error in the time evolution that stems from an inappropriate boson truncation is caused by the fact that the eigenvalues (energies) and eigenvectors of the untruncated Hamiltonian are poorly approximated. In Figure 3, we compare the energies of the ground state E_0 (the vacuum state) and the first excited state E_1 (the one-boson state) as a function of the interaction strength with different truncations. We find, that the first excited state is poorly approximated in the $N = 1$ scenario, which is not surprising, since the truncation should always be larger than the occupation number one wants to simulate. On the other hand, using a truncation of $\Lambda = 3$ ($N = 2$), we find excellent agreement with the ground state energy and also reasonably good agreement with the first excited state.

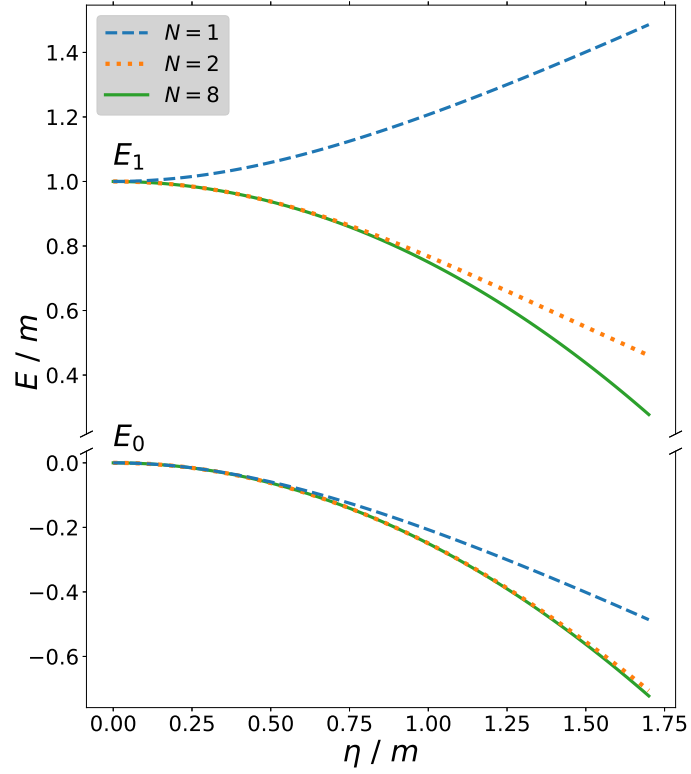


Figure 3: Energy-to-mass ratio E/m of the ground state and first excited state as a function of the coupling-to-mass ratio η/m . A truncation with $N = 1$ is insufficient to approximate the first excited state even at low coupling strengths. The truncation with $N = 3$ shows excellent agreement with the ground state and good qualitative agreement with the first excited state.

4 Circuit design

In the following we describe the design of quantum circuits emulating the dynamics of the system at hand. We start with the constant-depth two-qubit circuit that corresponds to the one-boson exchange case (Sec. 4.1), followed by its three-qubit counterpart in the case of three-boson exchange (Sec. 4.2). We then carry out a detailed analysis of the CNOT-cost estimate for higher boson-number truncations (Sec. 4.3). Finally, we present the basic aspects of a specific error-mitigation technique – the zero-noise extrapolation – that we will employ in this work (Sec. 4.4).

Before embarking on the construction of specific circuits, we point out how a specific property of the system at hand – namely, the local charge conservation – allows us to encode the fermion-antifermion sector of the problem using only one qubit. Starting from a general expression originating from the JW mapping, namely

$$a^\dagger a + c^\dagger c - 1 = \frac{1}{2} (IZ + ZI) = \begin{bmatrix} -1 & 0 & 0 & 0 \\ 0 & 0 & 0 & 0 \\ 0 & 0 & 0 & 0 \\ 0 & 0 & 0 & 1 \end{bmatrix}, \quad (20)$$

we restrict the system to the subspace with a total charge of $Q = 0$. Truncating the fermionic subspace to states with a vanishing total charge does not affect the behaviour of the system as the Yukawa interaction conserves the total charge and our chosen initial state, i.e. the vacuum state, has the total charge equal to zero. This allows us to rewrite $a^\dagger a + c^\dagger c - 1$ using only a single-qubit operator:

$$a^\dagger a + c^\dagger c - 1 = -Z. \quad (21)$$

This explains why the fermion-antifermion sector of the problem can be encoded using a single qubit.

Note that, in theory, one could completely spare the fermion-antifermion sector of the problem as the fermion- and antifermion numbers are separately conserved in our single-site model (one can see this from Eqs. (6) and (5), since both H_0 and H_{int} are diagonal in the fermion-number operator). Upon extension to multiple grid points with relativistic momenta, this would no longer hold, as only the charge remains conserved. This is the reason why we do not make use of the particle number conservation at this point and use the fermion-qubit as an additional source of noise.

4.1 Exchange of up to one boson (two-qubit circuit)

The next step is to apply both the fermion and boson mappings from Secs. 3.2 and 3.3, respectively, to obtain the qubit Hamiltonian. Here we truncate the bosonic occupation number at $\Lambda = 1$ such that $b + b^\dagger = X$. By making use of Eq. (21), the two contributions to the total qubit Hamiltonian $H_{\text{tot}} = H_0 + H_{\text{int}}$ are given by

$$H_0 = -M IZ - \frac{m}{2} ZI + \frac{1}{2} (2M + m), \quad (22)$$

$$H_{\text{int}} = -\frac{\eta}{2} XZ. \quad (23)$$

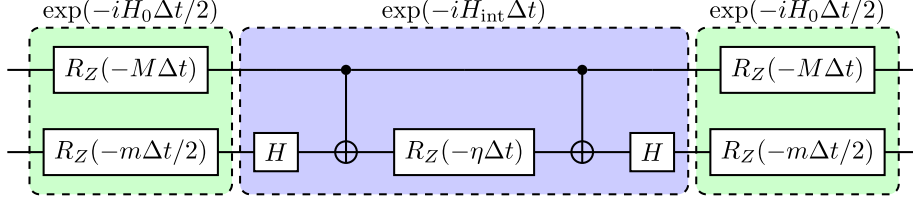


Figure 4: Circuit representing a Trotter step in the time evolution of the Hamiltonian $H_{\text{tot}} = H_0 + H_{\text{int}}$ [cf. Eqs. (22) and (23)].

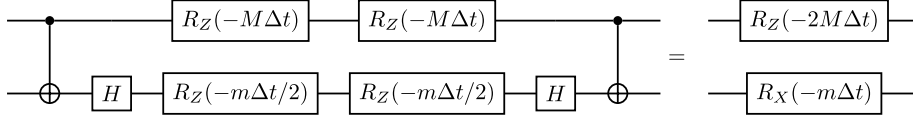


Figure 5: Circuit representation of the transition zone between two subsequent Trotter steps.

The spectrum of the free Hamiltonian H_0 is symmetrized by dropping the constant term $(2M + m)/2$. This changes the time evolution only by an irrelevant global phase.

The general approach to perform the time evolution of such a Hamiltonian with non-commuting terms is based on the Trotter-Suzuki decomposition, also known as Trotterization. To be more specific, for the Hamiltonian $H_{\text{tot}} = H_0 + H_{\text{int}}$ [cf. Eqs. (22) and (23)] our starting point is the standard second-order Trotter-Suzuki product formula [50, 51]

$$e^{-iH_{\text{tot}}\Delta t} = e^{-iH_0\Delta t/2}e^{-iH_{\text{int}}\Delta t}e^{-iH_0\Delta t/2} + O(\Delta t^3), \quad (24)$$

where the free Hamiltonian H_0 is used for symmetrization as its cost in terms of CNOT gates is zero. The circuit for a single Trotter step, based on the “star” configuration of CNOT gates [see Fig. 11(a)], is depicted in Fig. 4.

In the conventional scenario of using the product formula in Eq. (24), one obtains a quantum circuit whose depth scales linearly with the number of Trotter steps. In other words, the circuit depth grows with the total simulation time, which in many systems limits feasible simulations to relatively short times. We show that for the system at hand – at least in the two-qubit case (i.e. in the case of up to one boson exchange) – we can defy this conventional scenario and design a constant-depth circuit. To this end, it is instructive to start by analyzing the transition zone between subsequent Trotter steps, which is represented by the following circuit:

The simplification of the circuit in Fig. 5 is made possible by simple properties of the CNOT gate – namely, its commutation with a z -rotation gate on the control qubit and with an x -rotation gate on the target qubit, as well as the fact that the CNOT gate is self-inverse. It is also worthwhile pointing out that the occurrence of x -rotation gates on the target-qubit wire in the last circuit originates from the identity $R_X(\theta) = HR_Z(\theta)H$, which follows from the fact that $X = HZH$.

From this last circuit, one can easily go back to the exact time evolution by taking the limit $\Delta t \rightarrow 0$, $n \rightarrow \infty$ while keeping $n\Delta t \equiv t$ constant. This

approach yields the exact constant-depth quantum circuit that corresponds to infinitely many small time steps, i.e. to the finite evolution time t ; this circuit is shown in Fig. 6, where the top wire corresponds to the fermion, the bottom one to the boson. It should be emphasized that it is the specific form of the total Hamiltonian $H_{\text{tot}} = H_0 + H_{\text{int}}$ in Eqs. (22) and (23) that allows one to perform circuit compression between different Trotter steps such that only two CNOT gates are required to perform an arbitrary number of steps.

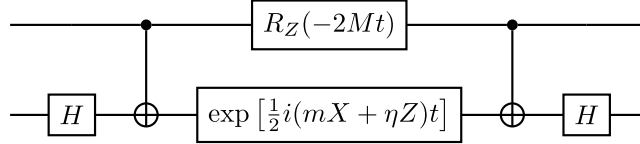


Figure 6: Exact constant-depth quantum circuit corresponding to the evolution governed by the Hamiltonian $H_{\text{tot}} = H_0 + H_{\text{int}}$ [cf. Eqs. (22) and (23)] over the finite time t .

At this point, the problem of decomposing the unitary two-qubit time-evolution operator has been reduced to the decomposition of a single-qubit gate. To this end, we recast $\exp[i(mX + \eta Z)t/2]$ by performing a ZXZ Euler decomposition $R_Z(\alpha)R_X(\beta)R_Z(\alpha)$, where

$$\begin{aligned}\alpha &= -\arctan\left[\frac{\eta}{\omega}\tan\left(\frac{\omega t}{2}\right)\right], \\ \beta &= -2\arctan\left[\frac{m}{\sqrt{\eta^2 + \omega^2 \cot^2\left(\frac{\omega t}{2}\right)}}\right],\end{aligned}\tag{25}$$

and $\omega^2 = m^2 + \eta^2$.

The final circuit, which emulates the system dynamics over a finite-evolution time t using only two CNOT gates, then assumes the form depicted in Fig. 7. In connection with the form of this circuit, it is worthwhile pointing out that circuit compressions of the type utilized here have quite recently been discussed in the context of interacting qubit arrays described by the transverse-field Ising- and XY models [48, 49], paradigmatic models in condensed-matter physics. These models can be mapped to free fermionic models and are also known to be classically simulatable with polynomial resources [67]. It is thus interesting that the fermion-boson system under consideration offers another, much less common example – namely, that of an XZ -coupled pair of qubits, with mutually unequal external fields in the z -direction acting on either qubit [cf. Eqs. (22) and (23)] – where such a circuit compression is also possible.

4.2 Exchange of up to three bosons (three-qubit circuit)

In order to describe an exchange of up to three bosons, two qubits are required to encode the bosonic Fock space. Using the bosonic qubit mapping, we modify

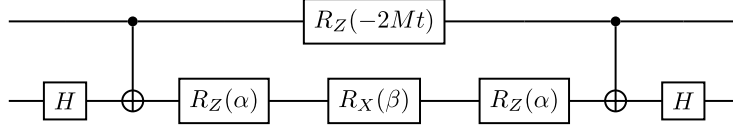


Figure 7: The full two-qubit circuit emulating the system dynamics in the one-boson-exchange case.

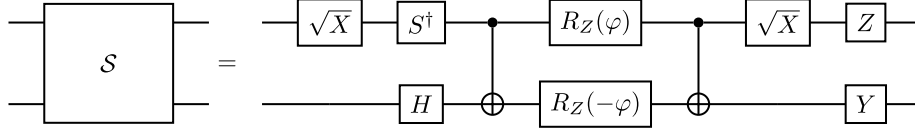


Figure 8: Minimal circuit representation of the unitary \mathcal{S} , obtained using the Kraus-Cirac decomposition.

the Hamiltonian as

$$H_0 = -M IIZ - \frac{m}{2} ZII - mIZI, \quad (26)$$

$$H_{\text{int}} = -\frac{\eta}{2} \left[\frac{1+\sqrt{3}}{2} XIZ + \frac{1-\sqrt{3}}{2} XZZ + \frac{1}{\sqrt{2}} (XXZ + YYZ) \right]. \quad (27)$$

To perform the time evolution of this Hamiltonian, we start with Trotterization. As this Hamiltonian does not allow for the same efficient circuit compression as in the one-boson case, we have to be more careful how to trotterize. To reduce the error of a Trotter step to $O(\Delta t^3)$, we once again make use of the second-order Trotter-Suzuki product formula [cf. Eq. (24)], also using the free Hamiltonian H_0 for symmetrization.

While a first-order Trotterization of $\exp(-iH_{\text{int}}\Delta t)$ requires 8 CNOT gates, we will instead construct an exact decomposition with the same gate count. The key idea is that H_{int} can be written as a tensor product of operators acting locally on the fermionic or bosonic registers. To calculate the matrix exponential, we may diagonalize these operators separately. The fermionic operator Z is already diagonal, leaving us with the task of diagonalizing $b + b^\dagger$. We find $b + b^\dagger = SDS^\dagger$, where in the matrix forms D and \mathcal{S} are given by

$$D = \text{diag}(-\lambda_+, \lambda_+, -\lambda_-, \lambda_-), \quad (28)$$

$$\mathcal{S} = \frac{1}{2} \begin{pmatrix} -\tilde{\lambda}_- & \tilde{\lambda}_- & \tilde{\lambda}_+ & -\tilde{\lambda}_+ \\ 1 & 1 & -1 & -1 \\ -\tilde{\lambda}_+ & \tilde{\lambda}_+ & -\tilde{\lambda}_- & \tilde{\lambda}_- \\ 1 & 1 & 1 & 1 \end{pmatrix}, \quad (29)$$

with $\lambda_\pm \equiv \sqrt{3 \pm \sqrt{6}}$ and $\tilde{\lambda}_\pm = \lambda_\pm / \sqrt{3}$.

The next step is to perform the Kraus-Cirac decomposition of \mathcal{S} , a transformation intimately related to the Cartan decomposition of the Lie algebra $su(4)$ [68, 69]. In this manner, we find that (for a detailed derivation, see Appendix C)

$$S = (K_4 \otimes K_3) \exp(i\varphi ZZ/2) (K_2 \otimes K_1), \quad (30)$$

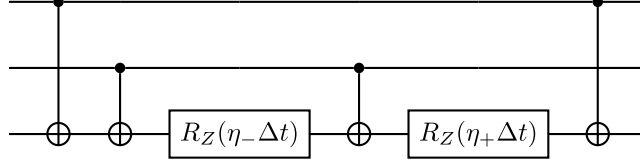


Figure 9: Quantum circuit representing $\exp(-iH_{\text{int, diag}}\Delta t)$.

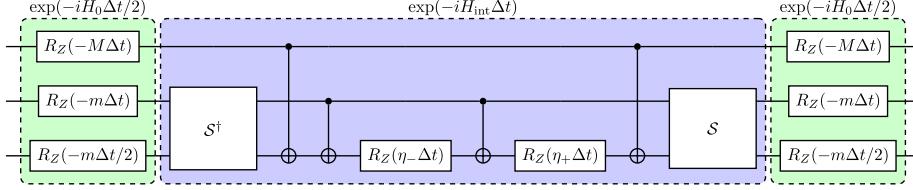


Figure 10: Quantum circuit for a single Trotter step in second-order Trotterization of the three-qubit Hamiltonian $H_{\text{tot}} = H_0 + H_{\text{int}}$ [cf. Eqs. (26) and (27)]. The bosonic register consists of the mid- and bottom wire.

where the matrices $K_1, \dots, K_4 \in \text{SU}(2)$ are given by

$$\begin{aligned}
K_1 &= \frac{e^{i\pi/4}}{\sqrt{2}} \begin{pmatrix} i & 1 \\ -i & 1 \end{pmatrix} = e^{-i\pi/4} S^\dagger \sqrt{X}, \\
K_2 &= \frac{e^{i\pi/2}}{\sqrt{2}} \begin{pmatrix} 1 & 1 \\ 1 & -1 \end{pmatrix} = \frac{e^{i\pi/2}}{\sqrt{2}} H, \\
K_3 &= \frac{e^{i\pi/2}}{\sqrt{2}} \begin{pmatrix} e^{-i\varphi} & -ie^{i\varphi} \\ ie^{-i\varphi} & -e^{i\varphi} \end{pmatrix} = e^{i\pi/2} Z \sqrt{X} R_Z(2\varphi), \\
K_4 &= \begin{pmatrix} 0 & -1 \\ 1 & 0 \end{pmatrix} = e^{i\pi/2} Y,
\end{aligned} \tag{31}$$

with $\varphi = \arctan[\sqrt{2}/(1 + \sqrt{3})]$. The minimal circuit representation of \mathcal{S} is depicted in Fig. 8.

The next step is to express D [cf. Eq. (28)] in the Pauli basis:

$$D = \sqrt{\frac{3 + \sqrt{3}}{2}} ZI + \sqrt{\frac{3 - \sqrt{3}}{2}} ZZ. \tag{32}$$

Then, the Hamiltonian H_{int} can be recast in the form

$$H_{\text{int, diag}} = \frac{1}{2}(\eta_- ZZZ + \eta_+ ZIZ), \tag{33}$$

where $\eta_{\pm} = \eta\sqrt{(3 \pm \sqrt{3})/2}$. The exact circuit for $\exp(-iH_{\text{int, diag}}\Delta t)$ is then given by Fig. 9.

Finally, by combining the circuits shown in Figs. 8 and 9 with those corresponding to the free Hamiltonian H_0 , we obtain the circuit that emulates a single Trotter step of the system under consideration. This circuit is depicted in Fig. 10.

4.3 CNOT-cost estimation for higher boson-number truncations

For simulations with higher truncation numbers (or more grid points), a more systematic approach towards circuit optimization is required due to the rapidly-increasing number of Pauli strings. Even when considering only a single grid point with a boson-number truncation at $\Lambda = 7$ (three bosonic qubits), circuit optimization by hand in the problem under consideration becomes rather tedious. Namely, for different possible orderings of Pauli strings, we obtain different CNOT-gate counts.

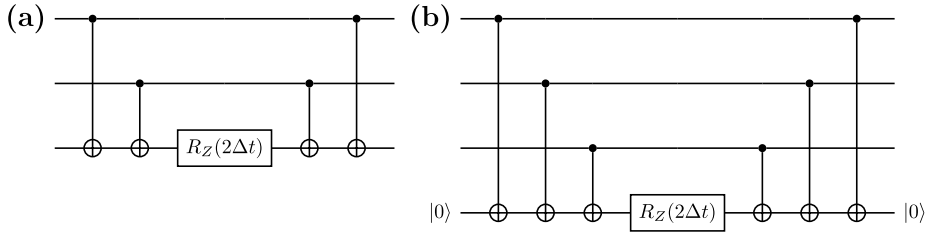


Figure 11: Quantum circuits for simulating the Hamiltonian $H = ZZZ$ for time δt using two different configurations of CNOT gates: (a) star configuration, and (b) star+ancilla configuration.

In what follows, we will focus on first-order Trotterization, which means that each Pauli string appears exactly once per Trotter step. All considerations in this section are based on the *star + ancilla* layout [64, 77], which is depicted in Fig. 11(b). Using this circuit layout, we can simulate the time evolution of any Hamiltonian of the form

$$H = \bigotimes_{k=0}^{n-1} \sigma_{c(k)}^k, \quad (34)$$

where $\sigma_{c(k)}^k \in \{I, X, Y, Z\}$ is a Pauli operator acting on the k -th qubit and H is given by a single Pauli string. The design of a quantum circuit emulating the time evolution governed by such a Hamiltonian is explained in Appendix E. For Hamiltonians with multiple non-commuting Pauli strings, we append the same circuit structure for each string and justify the circuit decomposition through the Trotter product formula.

Qubits with identity operations can be disregarded and qubits with X or Y are transformed to Z using $X = HZH$ and $Y = SHZHS^\dagger$. Whenever we deal with multiple non-commuting Pauli strings, we use Trotterization to recover the circuit structure from Fig. 11(b) for each string.

For the sake of simplifying the analysis of the CNOT-cost in this section, we ignore the fermionic qubit in the interaction Hamiltonian H_{int} , and focus entirely on the bosonic term $H_b \propto b + b^\dagger$. In other words, our goal is therefore to estimate the CNOT-cost of the circuit representation of $\exp(-iH_b\Delta t)$ for an arbitrary truncation Λ . We restrict ourselves to the case where the truncation can be expressed as $\Lambda = 2^N - 1$, where N is an integer corresponding to the amount of qubits forming the bosonic register. Let $S_N = \{P_1, P_2, \dots, P_k\}$ denote the set of Pauli strings required to encode $b + b^\dagger$. In Appendix D, we show that the

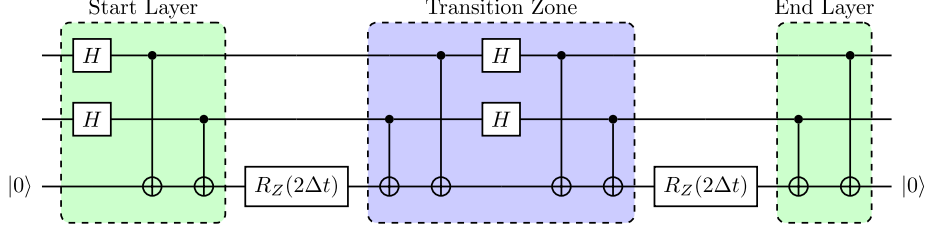


Figure 12: Time evolution circuit for the Hamiltonian $H = XX + ZZ$ using the Star+Ancilla layout. We define the zones on the left (right) of the first (last) R_Z -gate as the start (end) layer. A zone between two subsequent R_Z -gates is referred to as a transition zone.

number of Pauli strings k for a truncation to N qubits is given by

$$k = |S_N| = N2^{N-1}. \quad (35)$$

To find the optimal order of these strings, we use an approach based on an analogy with the TSP, adapting a technique proposed in Ref. [77]. The formulation of this optimization task as a TSP works as follows. We first define a weighted, fully-connected graph G with k nodes, where each node represents a Pauli string. We then set the edges between all nodes i and j with a weight given by $|P_i - P_j|_{\text{CNOT}}$, where $|P_i - P_j|_{\text{CNOT}}$ denotes the CNOT-cost to implement the transition between the circuits representing $\exp(-iP_i\Delta t)$ and $\exp(-iP_j\Delta t)$. A graphical illustration of the definition of the transition zone is provided in Fig. 12. In Appendix E we prove that the CNOT-cost to implement such a transition is precisely given by the Hamming distance

$$|P_1 - P_2|_{\text{CNOT}} := \sum_{i \in [N]} 1_{P_1[i] \neq P_2[i]} = |P_1 - P_2|_{\text{Ham}}. \quad (36)$$

Note that this distance metric differs by the one used in Ref. [77], since we take additional gate identities into account, which can significantly reduce the CNOT-cost, as explained in Appendix E.

TSP aims to minimize the cost of a closed path visiting all nodes exactly once. For a circuit made of k Pauli strings, there are $k - 1$ transition zones. A closed path on the graph described above would however consist of k transition zones. In Ref. [77], this issue is fixed by inserting an ancilla node which is connected to all nodes with zero weights. Note that this approach ignores the CNOT-cost of the start- and end-layers of the Trotterization circuit. In order to take also this cost into account, we find that the number of CNOTs to implement these layers is given by the Hamming weight

$$|P_j|_{\text{Ham}} = \sum_{i \in [N]} 1_{P_j[i] \neq I}. \quad (37)$$

Therefore, we use the above equation to calculate the weights for the edges connecting the nodes of the original graph with the ancilla node.

The closed path on our modified graph now contains $k + 1$ edges, of which two correspond to the start- and end layers, meaning that we have $k - 1$ transition zones, as desired.

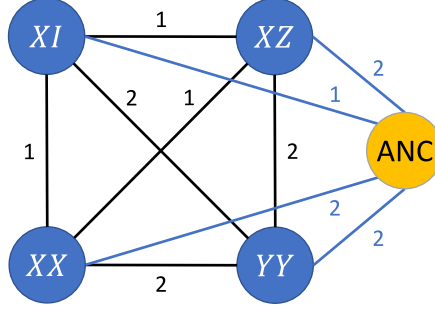


Figure 13: Graph representation of the set of Pauli strings $\{XI, XZ, XX, YY\}$. The weights between two Pauli string nodes (black edges) correspond to the Hamming distance (c.f. Eq. (36)), while the weight between a Pauli string node and the ancilla (ANC) node (blue edges) is the Hamming weight (c.f. Eq. (37))

Finally, to build the graph for the problem at hand, we need to know the Pauli strings explicitly. We generate the sets of Pauli strings recursively using

$$S_{N+1} = S_N \otimes I \cup S_N \otimes Z \cup S(\sigma_+^{\otimes N} \otimes \sigma_- + \sigma_-^{\otimes N} \otimes \sigma_+), \quad (38)$$

with $S_1 = \{X\}$, where the tensor product is performed element-wise (e.g., $S_N \otimes Z = \{P_1 \otimes Z, \dots, P_k \otimes Z\}$) and $S(O)$ denotes the set of Pauli strings building the operator O . A naive expansion of the last set $S(\sigma_+^{\otimes N} \otimes \sigma_- + \sigma_-^{\otimes N} \otimes \sigma_+)$ gives us 2^{N+1} different strings where each character can be either X or Y . But as the operator is Hermitian, all strings with imaginary coefficients cancel out. These strings are precisely the ones with an odd number of Y s. This leaves us with a subset containing 2^N strings with an even number of Y s. An example of the completed graph for a truncation with two qubits is shown in Fig. 13.

To solve the TSP exactly, we make use of the Bellman-Held-Karp dynamic-programming algorithm [55, 56], which scales in time with $\mathcal{O}(k^2 2^k)$. Due to the exponential growth of the number of Pauli strings, we are limited to truncations with $N \leq 3$ ($\Lambda \leq 7$). Because we are dealing with a metric graph, TSP can be 1.5-approximated in polynomial time $\mathcal{O}(k^3)$ using the Christofides algorithm [57]. We utilize this heuristic to approximate the CNOT-cost for truncations with $N \leq 8$ ($\Lambda \leq 255$). Finally, we compare the obtained results to an upper bound on the CNOT-cost derived in Appendix F. The results obtained using all three methods are illustrated in Fig. 14. While, needless to say, the Bellman-Held-Karp algorithm yields the best results, the Christofides heuristic outperforms the upper bound we propose. This suggests that a tighter bound on the CNOT-cost can be found.

4.4 Error mitigation by zero-noise extrapolation

Current NISQ devices, due to the limited number of qubits, do not allow one to perform full-fledged quantum error correction. As an alternative to error correction, various error-mitigation strategies have been proposed [80–86]. They all aim to identify the noiseless signal from a large number of noisy experimental repetitions.

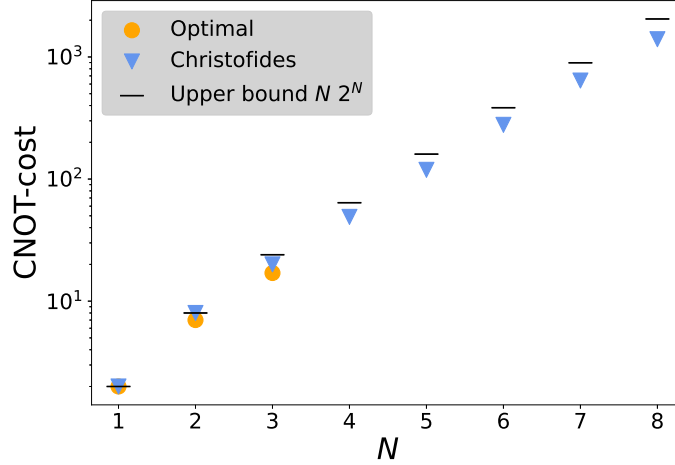


Figure 14: CNOT-cost for implementing the bosonic time evolution as a function of the qubit number N . Our algorithm achieves significant better results than the upper bound of $N 2^N$.

In the present work, we focus on one specific error-mitigation strategy, namely *zero-noise extrapolation* (ZNE) [82,83,87]. Much like other error-extrapolation methods, ZNE make use of expectation values $E(\lambda)$, obtained at multiple different physical noise levels that are quantified by the dimensionless scale factor λ (where $\lambda = 1$ is the actual noise level of the physical hardware), to infer the noiseless expectation value $E(\lambda = 0)$.

The basic idea of ZNE is to scale the noise of a quantum computation by means of *unitary folding*, i.e., replacing a unitary circuit U by

$$U \rightarrow U(U^\dagger U)^n, \quad (39)$$

where n is a positive integer. While in an ideal circuit – where $U^\dagger U = \mathbb{1}_D$, with D being the dimension of the Hilbert space associated to all the qubits of the circuit – this folding operation has a trivial effect, one can expect that on a realistic (noisy) quantum computer the same operation amounts to increasing the noise.

The unitary folding can be implemented in the guise of *circuit folding* and *gate folding*, where the latter has its left and right versions. To illustrate these different types of unitary folding, let us assume that we have a quantum circuit emulating the time evolution of a system, where each Trotter step (corresponding to the time δt) is described by the unitary U . Then, e.g., the state of the system at time $t = 3\delta t$ is given by $|\psi(t)\rangle = UUU|\psi(t=0)\rangle$. In the circuit folding, we are replacing UUU by $UUU(U^\dagger U^\dagger U^\dagger)UUU$ (first order) or by $(UUU(U^\dagger U^\dagger U^\dagger)UUU)^2$ (second order). In the gate folding from left, we are replacing UUU by $UU^\dagger UUU$ (first order) or $UU^\dagger UUU^\dagger UU$ (second order). Finally, in the gate folding from right we are replacing UUU by $UUUU^\dagger U$ (first order) or $UUU^\dagger UUU^\dagger U$ (second order).

Assuming that the noise model for the relevant quantum circuit is that of a global depolarizing channel [64], the density matrix of the system can be

represented as

$$\rho \xrightarrow{\text{noisy circuit}} p U \rho U^\dagger + (1 - p) \mathbb{1}_D / D, \quad (40)$$

where $p \equiv \prod_j p_j$ is the product of the gate-dependent noise parameters $p_j \in [0, 1]$ for all the gates in the given circuit. If all the input gates are folded exactly n times (the corresponding value of the scale factor is $\lambda = 2n + 1$), in both the circuit- and gate-folding cases one obtains

$$\rho \xrightarrow{\text{noisy + unitary folding}} p^\lambda U \rho U^\dagger + (1 - p^\lambda) \mathbb{1}_D / D, \quad (41)$$

i.e., an exponential scaling – in terms of the noise level λ – of the depolarizing parameters p_j for each gate ($p_j \rightarrow p_j^\lambda$). Therefore, under the aforementioned initial assumption of depolarizing channel (which commutes with unitary operations) the unitary folding amounts to an exponential dependence of any expectation value $E(\lambda)$:

$$E(\lambda) = a + b p^\lambda. \quad (42)$$

The coefficients a and b can be determined by fitting the obtained numerical results to the last exponential Ansatz, which is followed by a straightforward extrapolation to the noiseless case ($\lambda = 0$).

5 DQS on IBM Q: Results and Discussion

In what follows, we present and discuss the results obtained by running the designed quantum circuits emulating the system dynamics – both for the cases of up to one and three boson-exchange processes – on IBM Q. We start with the results obtained for the Loschmidt echo (Sec. 5.1). We then present the results obtained for boson occupation numbers (Sec. 5.2) and adiabatic state preparation (Sec. 5.3).

We benchmark the accuracy of our DQS by comparing the results obtained on the IBM Q processor [42] `ibmq_manila` with those resulting from a numerically-exact treatment of the quantum dynamics governed by the truncated Hamiltonians of the model under consideration on a classical computer.

To demonstrate that our simplified, single-site model of scalar Yukawa coupling exhibits nontrivial quantum dynamics, we perform DQS of this model taking the vacuum state as the initial state of the fermion-boson system. We construct the states $|\psi(t)\rangle$ of the system at different times t by applying the designed two- and three-qubit circuits that emulate the system dynamics following a Yukawa-interaction quench at $t = 0$. Finally, for each of those constructed states we perform measurements that give us access to the desired quantities, bearing in mind the relevant expressions in the Pauli basis [cf. Eqs. (14) and (19)].

Given that the DQS of the single-site fermion-boson model under consideration only requires two- and three-qubit systems [cf. Sec. 4], for benchmarking purposes it was sufficient to make use of the freely available, five-qubit processor `ibmq_manila` [42].

The qubit-connectivity graph (coupling map) of this quantum processor, with the corresponding enumeration of physical qubits, is depicted in the left panel of Fig. 15

Generally speaking, the errors in numerical experiments on IBM Q devices strongly depend on the number of CNOT gates in the corresponding quantum

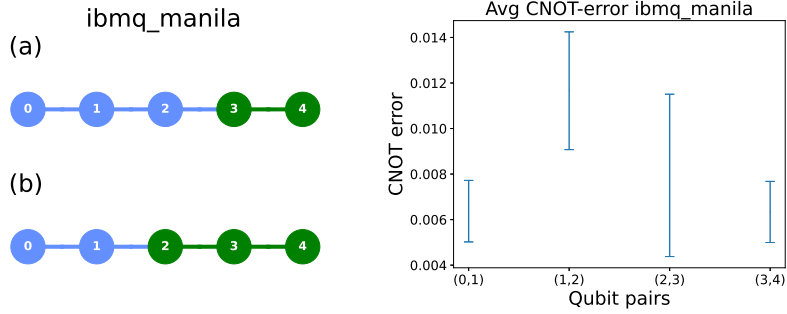


Figure 15: Left panel: Qubit-connectivity graphs (coupling maps) of `ibmq_manila` for (a) two-qubit case (with qubits 3 and 4 used in the actual implementation), and (b) three-qubit case (with qubits 2, 3, and 4 used in the implementation). Right panel: CNOT gate errors for `ibmq_manila` averaged over calibration data from January to April 2023.

circuit. The principal reason for this is that the CNOT-gate error is an order of magnitude larger than that of single-qubit gates. Another reason is that the CNOT-gate time is much longer than that of its single-qubit counterparts, which leads to the accumulation of errors due to energy relaxation and dephasing, this two processes being quantified by the respective decoherence times T_1 and T_2 [4]. Therefore, in order to minimize the error, in our DQS we make use of the connected subsets of qubits with the smallest average CNOT error according to the calibration data from Ref. [42]. In the right panel of Fig. 15 we show the average CNOT error averaged over calibration data from January to April 2023. As can be inferred from this plot, the qubit pairs (0, 1) and (3, 4) have roughly the same error rates. However, for our three-qubit circuits it is beneficial to use the qubit pair (2, 3) instead of (1, 2).

The simulation parameters used for the following benchmarks are $M/m = 7$ (nucleon/pion mass ratio), $\eta/m = 1.7$ and $t_0 \equiv 1/\sqrt{m^2 + \eta^2}$. For the calculations of all the following observables, we use the *Estimator primitive* as well as the *Sampler primitive* provided in `qiskit_runtime` [58]. This allows to use post-correction of all observables. We set `resilience_level = 1`, which performs a readout error correction on the measured observable. We ran each circuit on the IBM Q processor with 8192 shots.

5.1 Loschmidt echo and state fidelity

We start by evaluating the Loschmidt echo, which in the problem under consideration is given by [cf. Eq. (7)]

$$\mathcal{L}(t) = |\langle \psi_{t=0} | e^{-i(H_0 + H_{\text{int}})t} | \psi_{t=0} \rangle|^2, \quad (43)$$

by performing the reconstruction of the state of the system at time t using quantum-state-tomography algorithms [74]. In the problem at hand, the time-evolution (DQS) circuits [cf. Sec. 4] – which emulate the dynamics governed by the total Hamiltonian $H_{\text{tot}} = H_0 + H_{\text{int}}$ of the system after a Yukawa-interaction quench at $t = 0$, starting from the initial state $|\psi_{t=0}\rangle \equiv |\psi_0\rangle$ – play the role of the required state-preparation circuits.

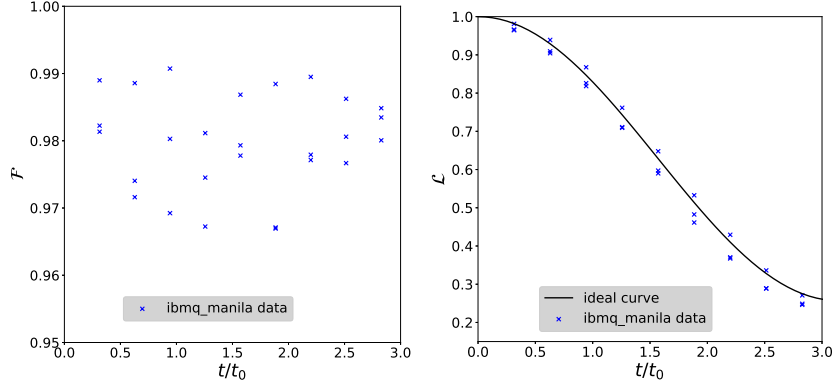


Figure 16: State fidelity \mathcal{F} (left panel) and Loschmidt echo \mathcal{L} (right panel) as function of the dimensionless time t/t_0 for the two-qubit circuits. The fidelity remains constantly high during the whole simulated time interval, which is a consequence of the constant depth circuit construction. The measured Loschmidt echo shows excellent agreement with the theory curve. Each experiment was repeated three times.

Generally speaking, the objective of quantum-state tomography is to reconstruct the density matrix ρ that corresponds to the actual state of the system [64, 70, 71]. Because our quantum circuits do not involve any measurements, the state of the system can be described using the state-vector formalism (recall that the density matrix corresponding to the pure state $|\psi\rangle$ is given by $\rho = |\psi\rangle\langle\psi|$). In general, to carry out quantum-state tomography on an N -qubit system one has to perform 3^N measurements for a generic mixed state [72, 73].

Throughout this work, we used the pre-implemented tomography method from the `qiskit-experiments` package [75], which comes with different tomography fitters. More specifically, we used the `linear_inversion` fitter, based on the work of Ref. [74], which is an efficient method for computing the maximum-likelihood quantum state given a set of measurement outcomes in a complete orthonormal operator basis.

Given the reconstructed density matrix of the final state, as well as the density matrices of the initial state and the ideal final state (obtained through classical simulation), we compute the Loschmidt echo and the fidelity of the evolved state starting from the general expression for the quantum-state fidelity [76]

$$\mathcal{F}(\rho, \sigma) = \left(\text{Tr}(\sqrt{\sqrt{\rho} \sigma \sqrt{\rho}}) \right)^2, \quad (44)$$

where ρ and σ are the density matrices of the two mixed quantum states. In the special case of pure states – of interest in the problem at hand – the last general expression reduces to $\mathcal{F}(\rho, \sigma) = |\langle\psi_\rho|\psi_\sigma\rangle|^2$ (here $\rho \equiv |\psi_\rho\rangle\langle\psi_\rho|$ and $\sigma \equiv |\psi_\sigma\rangle\langle\psi_\sigma|$ are the density matrices corresponding to the pure states $|\psi_\rho\rangle$ and $|\psi_\sigma\rangle$, respectively).

In the following we make use of two different simulation schemes in order to increase the truncation number in the time evolution of the system. In the first one (*static truncation*), we use the same boson-truncation throughout the entire

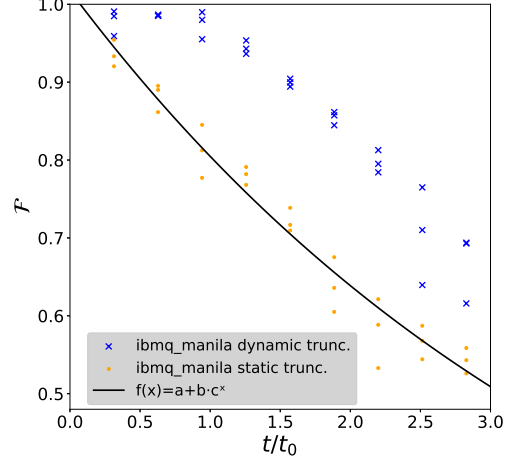


Figure 17: State fidelity \mathcal{F} as a function of the dimensionless time t/t_0 comparing the dynamic with the static truncation. As can be seen, the fidelity for the dynamic truncation circuits stays on a plateau for the first three steps, for which we used the two qubit circuits, and then starts to fall. The decrease of the fidelity can be explained by the increase of noise in the circuit. We fit this decrease using an exponential model, from which we can deduce the average CNOT gate errors of `ibmq_manila`.

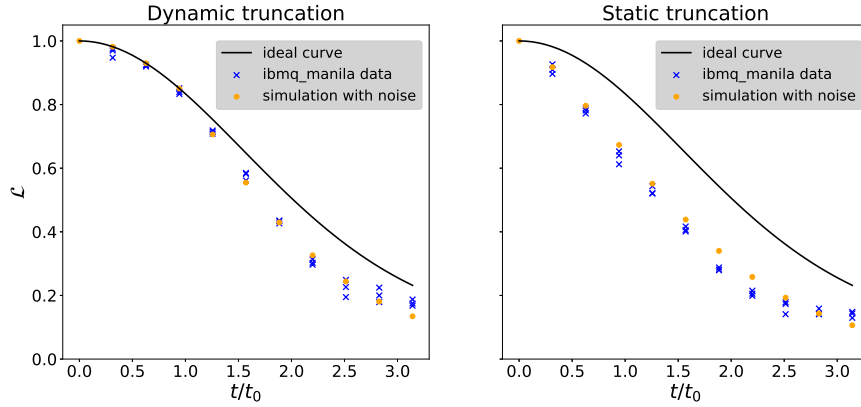


Figure 18: Loschmidt echo \mathcal{L} as a function of the dimensionless time t/t_0 for the dynamic truncation time-evolution (left panel) and the static truncation time-evolution (right panel). The data from the quantum computer (blue crosses) is shifted compared to the ideal theory curve. This shift can be explained by polarization noise, which we modeled according to Eq. (40) (orange dots).

time evolution process. In the second one (*dynamic truncation*) we start the time evolution with a lower truncation number (here $N = 1$) and then increase after a critical time, according to Fig. 1. While, in principle, this increases the overall truncation error, the effect is negligible compared to the benefit of simulating time steps with lower-depth circuits.

In our *dynamic truncation* simulation scheme, we use the two-qubit circuit for the first three time steps, and append the Trotterized three-qubit circuit starting from the fourth time step. We increase the truncation earlier than indicated in Fig. 1, since we want to reach a state fidelity much higher than 90% at the point where the truncation is increased, such that the target accuracy of 90% can be achieved in the end.

The obtained results for the state fidelities are shown in Figs. 16 (left panel) and 17 for the two- and three-qubit circuits, respectively. We repeat each measurement three times. As expected, for the two-qubit circuits the fidelity remains constant at roughly 0.98 on average for all ten time steps. This is the effect of our constant-depth circuit (i.e. circuit compression), leading to a high fidelity at all times. For the three-qubit case we observe a fast decrease of the state fidelity from the beginning in the static truncation simulation, while for the dynamic truncation this decrease starts after 3 steps only, when we have to use the three-qubit circuits to simulate the system. This decrease of the fidelity can be attributed to the increase of noise in the quantum circuit when more gates are ad. Under the assumption of a depolarization model [cf. Eq. (40)], the fidelity drop can be fit with an exponential function,

$$f(n) = a + b \cdot c^n, \quad (45)$$

where n is the number of time steps. From the value of c one can estimate the average error of applying the unitary evolution for one time step, which is given by $1 - c$. From our fit, we find

$$c = 0.925 \pm 0.025. \quad (46)$$

Since the unitary in the three-qubit case consists of 8 CNOT gates, we can estimate the average CNOT gate-error, which is roughly 0.008 ± 0.003 , which indeed is in line with the reported calibration data (cf. Fig. 15).

In the right panel of Fig. 16 and Fig. 18 we show the results for the Loschmidt echo for the two- and three-qubit circuits. In the two-qubit case we find very good agreement between the ideal theory curve and the experimental data from the quantum processor. For the three-qubit case we find a deviation, which increases with the number of time steps, as expected due to the accumulation of noise. Using the fit-parameter from the fidelity experiments, we try to model the effect of depolarization noise on the Loschmidt echo (orange points in Fig. 18). We do this by calculating the noisy Loschmidt echo with the depolarized density matrix

$$\rho \rightarrow c^n \rho + \frac{(1-c)^n}{3} \mathbb{1}_{3 \times 3}, \quad (47)$$

where c is given by Eq. (46) and n denotes the n -th step. As can be seen from that plot, this model can qualitatively describe the deviation from the data compared to the ideal theory curve in the dynamic truncation time evolution as well as in the static one.

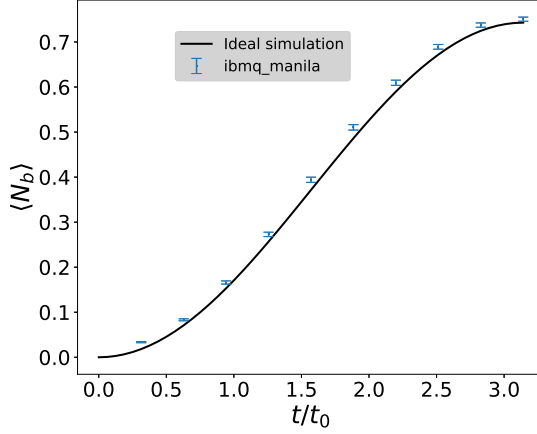


Figure 19: Expected boson number $\langle N_b \rangle$ as a function of the dimensionless time t/t_0 using one bosonic qubit. The error bars correspond to shot noise assuming a Gaussian distribution.

5.2 Boson occupation numbers

The obtained results in the two-qubit case are illustrated in Fig. 19, which shows the expectation values of the boson-number operator at an arbitrary time t after the quench. As can be seen, the compressed circuit with only two CNOT gates [cf. Sec. 4.1] shows excellent agreement with the exact (continuous-time) quantum dynamics. The error-bars shown in Fig.19 show the effect of shot noise in the quantum computation under the assumption of a normal distribution.

As derived in Sec. 3.4, the truncation error of the two-qubit simulation (i.e., one bosonic qubit) exceeds the accuracy-threshold of 10% during the simulated time interval (cf. Fig. 1). However, as also shown in this figure, a truncation with two bosonic qubits is sufficient to simulate the system with a fidelity of 90% in the time interval of interest.

We now proceed to extend our two-qubit time-evolution circuit to a three-qubit system with two bosonic qubits. We compare the results of dynamic and static truncation, allowing up to three bosons exchanged, in Fig. 20. As can be inferred from this plot, the dynamic truncation approach offers a significant improvement compared to the naive static truncation for the raw data: the first three data points, for which we used the two-qubit circuits, are – as expected – in a very good agreement with the theory curve. From step 4 onwards we observe a large deviation, similar to what happens in the static truncation case from the beginning of the evolution.

Even with the dynamic truncation we find a significant deviation between the theory curve and the data simulated by the quantum computer for larger time steps. In order to improve our results and reduce the error we use the ZNE technique [cf. Sec. 4.4]. We tried three different unitary folding schemes in order to perform the extrapolation: gate folding from left, from right, and circuit folding. We found that circuit folding works the best for our problem and show the accumulated data for this approach in Figs. 21 and 22.

We ran each experiment three times and used the data to perform a linear

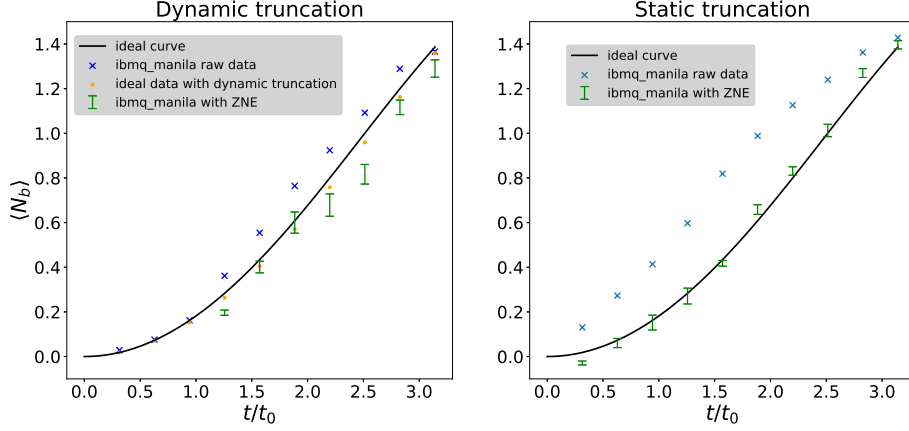


Figure 20: Expected boson number $\langle N_b \rangle$ as a function of the dimensionless time t/t_0 for dynamic truncation (left panel) and static truncation (right panel) circuits. While for the raw data the dynamic truncation scheme gives much better results than the static truncation, the ZNE is able to reproduce the expected data quite well in both cases.

extrapolation to the zero-noise limit. In Figs. 21 and 22 we plot the number of CNOT gates vs. the measured bosonic occupation number. As can be seen, an increase in the number of CNOT gates leads to an increase of the occupation number due to more noise in the quantum circuit. At some point (more precisely, around a total number of 200 CNOT gates) the curve saturates at a value of $\langle N_b \rangle = 1.5$. This is expected, since in the three-qubit case we have [cf. Eq. (19)]

$$\langle N_b \rangle = 1 - \langle Z_1 \rangle + \frac{1 - \langle Z_0 \rangle}{2}. \quad (48)$$

For a completely depolarized quantum device, we have $\langle Z_i \rangle = 0.5$ and thus $\langle N_b \rangle = 1.5$. According to the calibration data of `ibmq manila` [42], the average dephasing time T_2 of the device is around $70 \mu s$. Dividing the T_2 time by the average CNOT gate-time of $350 ns$, we obtain an estimate for the number of CNOTs that can be performed on the device:

$$N_{\text{CNOT}} = \frac{70 \mu s}{350 ns} = 200. \quad (49)$$

The obtained expected number of CNOTs agrees very well with our own findings about the maximal number of CNOT gates that can be executed before the device gets completely depolarized.

We perform the ZNE using linear extrapolation by performing a linear least-square fit to the data. The error bars in Fig. 20 are given by the standard deviation of the intercept that we extract from the fit. Since the noise only increases linearly with the number of CNOTs up to a certain point, we select by hand only those points that are below the observed threshold and use them to perform our extrapolation.

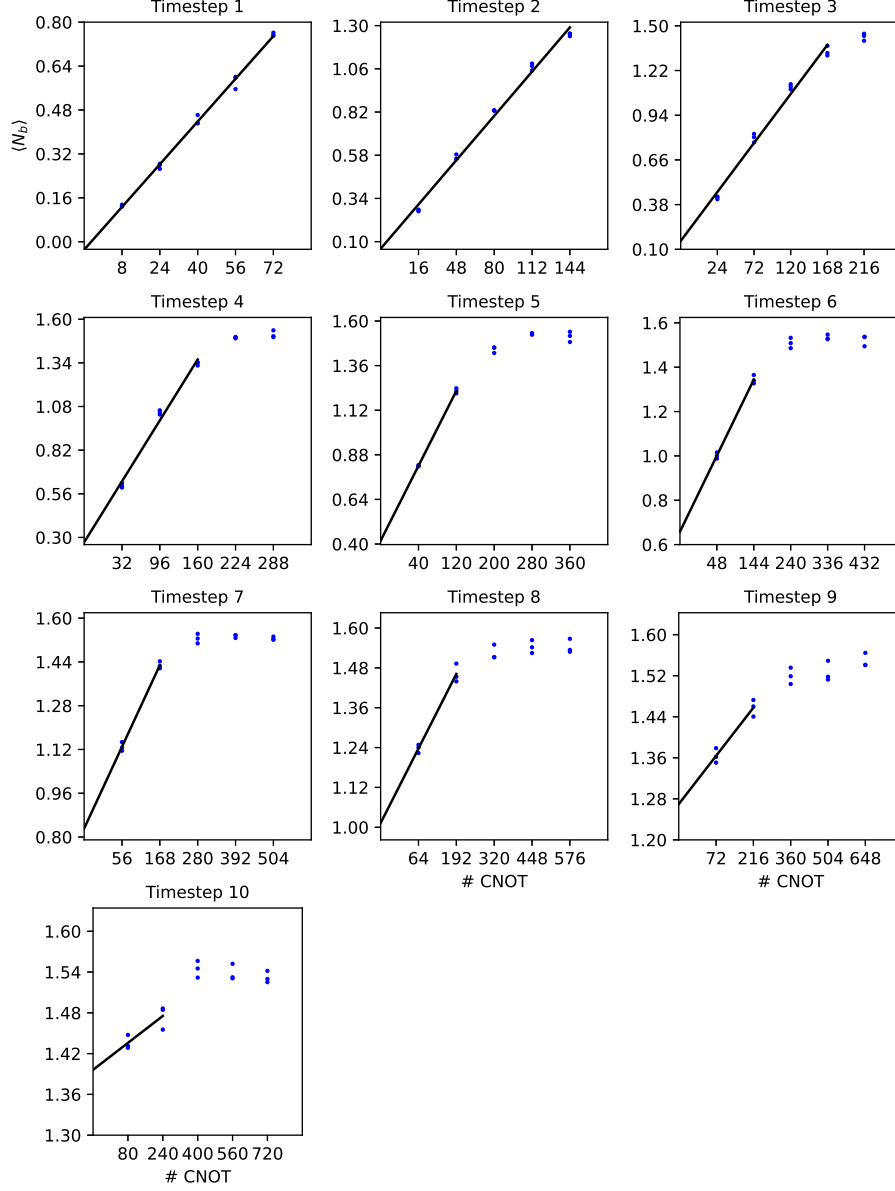


Figure 21: ZNE for the static truncation using three qubits in all time steps. We repeated each experiment three times (blue dots). On the y axis we show the measured bosonic occupation number and on the x -axis the total number of CNOT gates per circuit. We use the data to extrapolate to the noiseless limit (solid line). It is evident that for circuits with a CNOT number bigger than 200, the occupation number saturates at $\langle N_b \rangle = 1.5$. This is expected, given that a completely depolarized device, which generates random bit-strings, would yield that value.

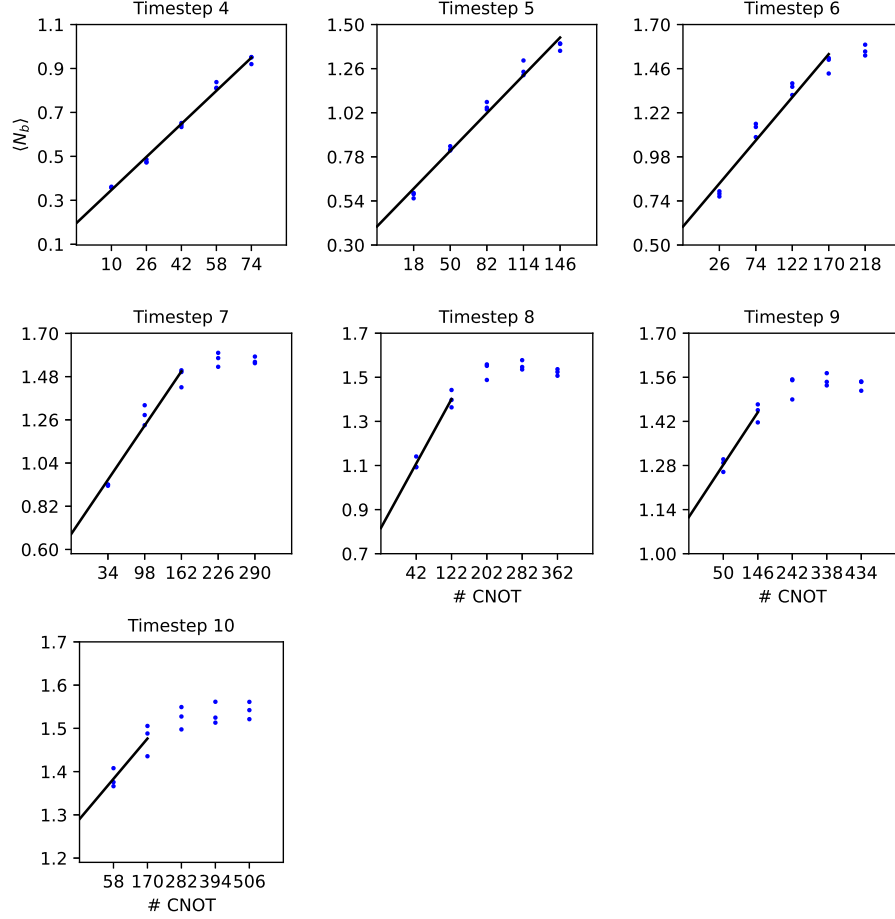


Figure 22: ZNE for the dynamic truncation. On the y axis we show the measured bosonic occupation number and on the x -axis the total number of CNOT gates per circuit. Each experiment is repeated three times (blue dots). We use the data to extrapolate to the zero-noise limit (solid line). The first three time steps are performed using a two-qubit circuit, for which ZNE is not necessary. Thus, the data for these time steps is not shown here.

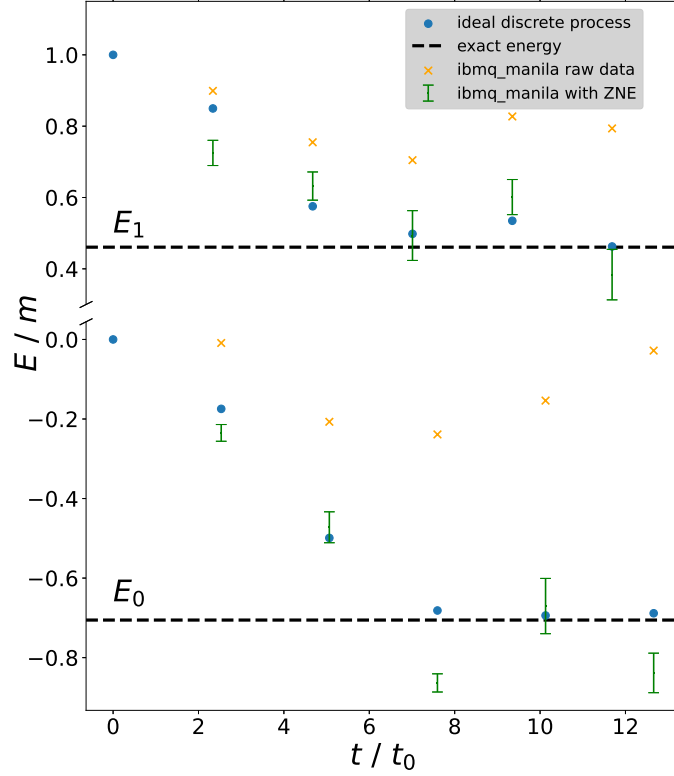


Figure 23: Energy-to-mass ratio E / m as a function of dimensionless time t / t_0 during the adiabatic processes preparing the ground state and first excited state of the interacting theory.

5.3 Adiabatic preparation of the ground- and first-excited states

In this section, we apply the time-evolution circuits to eigenstates of the free Hamiltonian H_0 to drive them adiabatically to eigenstates of the interacting theory, described by $H = H_0 + H_{\text{int}}$ [cf. Eqs. (5) and (6)].

Adiabatic state preparation is based on the adiabatic theorem of quantum mechanics [44]: a system which is in an eigenstate of a time-dependent Hamiltonian $H(t) = H_0 + H_{\text{int}}(t)$ at an initial time t_0 , such that its time evolution is governed by the Schrödinger equation

$$i \frac{\partial}{\partial t} |\psi(t)\rangle = H(t) |\psi(t)\rangle, \quad (50)$$

will remain an eigenstate, provided that the change of $H(t)$ is “sufficiently slow.” (For an up-to-date review in the quantum-computing context, see Ref. [45]).

For our experiments we made use of the fact, that the fermionic particle number is conserved during the whole adiabatic process. We thus do not need to measure the fermionic qubit, although we keep it in the circuit as an additional source of noise like before. The bosonic Hamiltonian, for which we consider the

adiabatic transition is thus given by [cf. Eq. (27)]:

$$H_b = -\frac{m}{2} ZI - m IZ - \frac{\eta}{2} \left[\frac{1+\sqrt{3}}{2} XI + \frac{1-\sqrt{3}}{2} XZ + \frac{1}{\sqrt{2}}(XX + YY) \right] + \frac{3}{2}m, \quad (51)$$

and we consider the full Hamiltonian is: $H = H_b \otimes \mathbb{1}_f$, where $\mathbb{1}_f$ denotes the identity operator acting on the fermionic qubit.

In order to find the ground state and the first excited state of the interacting single-site Yukawa theory, we start from the corresponding eigenstates of H_0 in Eq. (6). These states can straightforwardly be prepared as H_0 is already diagonal. For instance, to prepare the state with one boson, we simply flip the corresponding qubit in the bosonic register using an X -gate.

Once the desired eigenstate of H_0 is prepared, we drive an adiabatic transition using the same quantum circuit as for the time evolution in the three-qubit case (Fig. 10), the only difference being that we increase the coupling strength η with each time step.

Ideally, one would choose a large time interval divided into a large number of small steps in order to steadily increase coupling. However, as evident from the benchmarks of the state fidelity in Fig. 17, the state fidelity decreases significantly with each time step. Hence, we aim to perform the adiabatic transition using only 5 time steps, expecting to keep the fidelity of the final state on `ibmq_manila` above 70%. At the same time, the length of a time step is limited due to the Trotter error. Consequently, we make use of classical computation to determine the optimal time step Δt , taking the Trotter error into account, to achieve the best possible final state within five steps.

The optimised discrete processes for both states of interest, are illustrated in Fig. 23. We find that a total simulation time of roughly $t \approx 13 t_0$ is enough to drive the system adiabatically into the eigenstates of the interacting theory. Discretizing that time into five time steps of the length $\Delta t = 2.53 t_0$ (ground state) and $\Delta t = 2.34 t_0$ (first excited state), suffices to achieve fidelities of the final state of about 99% for both states under consideration (blue dots in Fig. 23).

From calculating the state fidelities on `ibmq_manila` in the previous section we know that even only these five time steps are too many to produce meaningful results due to the accumulated gate errors. For this reason we again employ our ZNE protocol to reduce the errors of the quantum circuits. In Fig. 24 we show the data accumulation in order to perform the ZNE. Like before, we repeated each experiment three times and used linear extrapolation to get the zero-noise limit of the bosonic Hamiltonian. As in the case of the bosonic expectation value in Sec. 5.2 we find an increase in the expectation value by adding additional noise. The energy saturates at an expectation value of $\langle H \rangle_b / m = 1.5$ after roughly 200 CNOT gates. This is expected, since the three-qubit Hamiltonian has a constant term $H_b \propto 1.5m$.

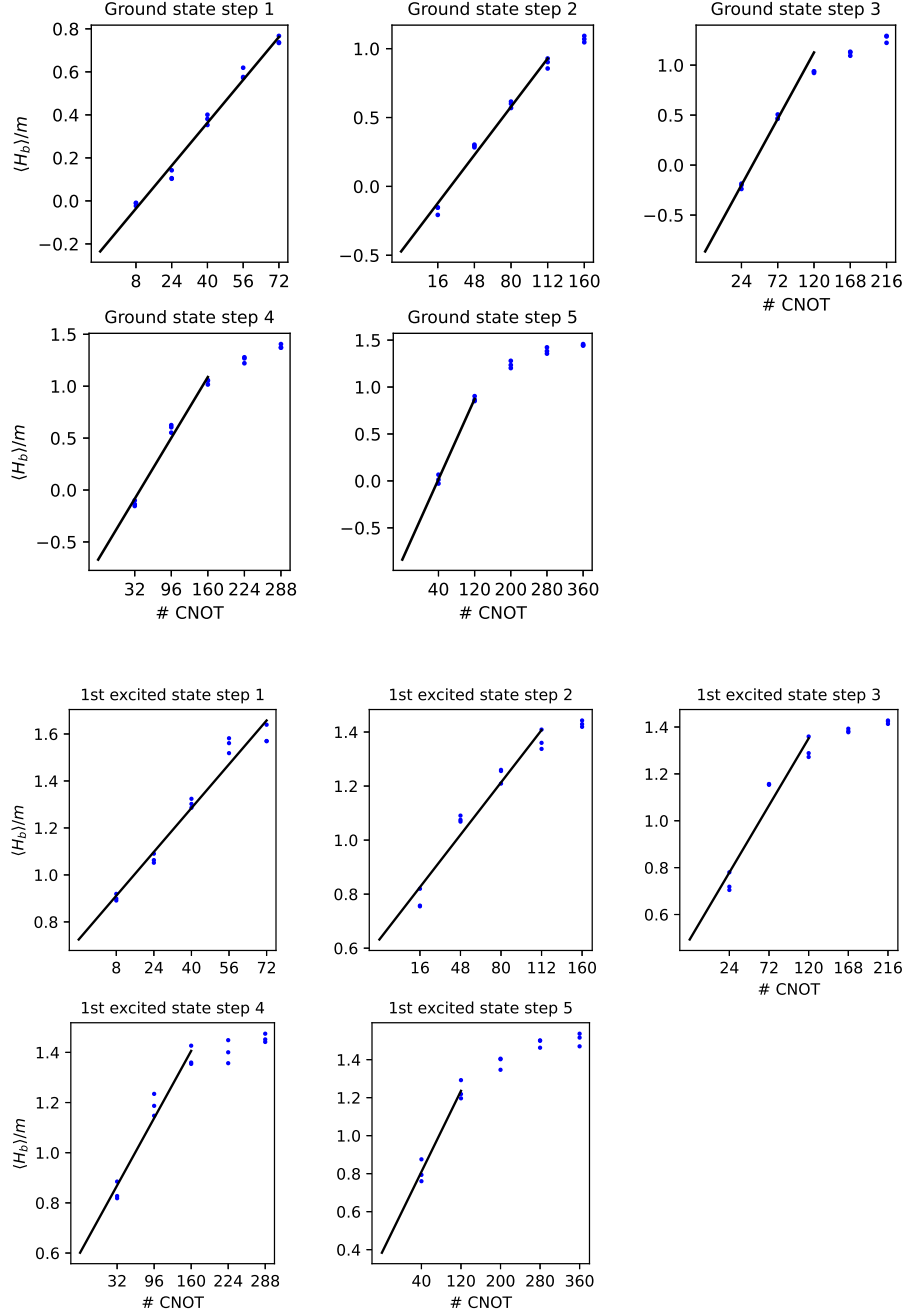


Figure 24: ZNE for measuring the energies of the ground state (upper panel) and the first-excited state (lower panel). Each experiment is repeated three times (blue dots). By adding more CNOT gates into the circuit, the expectation value of H_b/m saturates at the value 1.5. Like for the bosonic occupation number, we select the region for extrapolation by hand, where the increase due to noise seems to be linear (solid line).

6 Summary and Conclusions

To summarize, in this paper we investigated the non-equilibrium dynamics of a coupled fermion-boson system following a quench of Yukawa-type interaction and calculated the two lowest energies of the spectrum of the interaction Hamiltonian within the framework of digital quantum simulation. In particular, we showed that a single-site abstraction of scalar Yukawa coupling can successfully be simulated on the existing **IBMQ** hardware in the regime of low boson-number exchange.

Using advanced circuit-optimization techniques – exemplified by the Kraus-Cirac decomposition – we designed efficient, low-depth quantum circuits for simulating the exchange of up to three bosons. In particular, in the one-boson case we designed a constant-depth circuit with only two CNOT gates, regardless of the total simulation time. This constitutes an example of circuit compression, which is only possible for certain special types of the underlying system Hamiltonian and allows one to defy the usual linear scaling of the circuit depth with the number of Trotter steps. In the three-boson case – where such a compression is no longer possible – we designed a circuit in which one Trotter step requires 8 CNOT gates, which is far below the maximal CNOT-cost of an arbitrary three-qubit gate (14 CNOTs) [52]. Finally, by making use of an analogy with the travelling salesman problem, we also derived a CNOT-cost estimate for quantum circuits emulating the system dynamics for higher boson-number truncations.

Based on the designed circuits we computed the expected boson numbers at an arbitrary time after the quench. By performing state reconstruction using quantum-state-tomography algorithms, we recovered the Loschmidt echo, a quantity that characterizes the survival probability of the initial state of the system, and calculated the fidelities of the quantum circuits. Finally, we successfully reproduced an adiabatic process to compute the two lowest eigenvalues of the interacting theory, using the designed time-evolution circuits. Using the zero-noise extrapolation technique, one of the most widely used error-mitigation approaches, we demonstrated an excellent agreement of our obtained results with numerically-exact classical benchmarks.

The findings of the present study are likely to motivate future work in several different directions. For example, it is of interest to extend our single-site digital quantum simulation to multi-site realizations, including much larger systems for which benchmarking may require access to quantum devices with a smaller two-qubit gate error and all-to-all connectivity [78]. For such systems, tensor networks may provide an efficient approximation for certain classes of quantum states [79]. Finally, accurate simulations of larger systems might be enabled through the use of circuit-optimization techniques based on machine learning [88].

Acknowledgments

The authors would like to acknowledge useful discussions on the field-theoretical description of Yukawa coupling with H.-W. Hammer. This research was supported in part by the Deutsche Forschungsgemeinschaft (DFG) – SFB 1119 – 236615297 (G. A. and V. M. S.) and in part by the research project “Zentrum

für Angewandtes Quantencomputing" (ZAQC), which is funded by the Hessian Ministry for Digital Strategy and Innovation and the Hessian Ministry of Higher Education, Research and the Arts (T. N. K. and M. H.). We acknowledge the use of IBM Quantum services for this work. The views expressed are those of the authors, and do not reflect the official policy or position of IBM or the IBM Quantum team.

A Derivation of the single-site Hamiltonian

A.1 Free Hamiltonian

The free Hamiltonians of the Dirac- and Klein-Gordon fields in momentum space are given by

$$\begin{aligned} H_{\text{Dirac}} &= \int \frac{d^3p}{(2\pi)^3} \Omega_{\mathbf{p}} \sum_s (a_{\mathbf{p}}^{s\dagger} a_{\mathbf{p}}^s + c_{\mathbf{p}}^{s\dagger} c_{\mathbf{p}}^s) , \\ H_{\text{KG}} &= \int \frac{d^3p}{(2\pi)^3} \omega_{\mathbf{p}} b_{\mathbf{p}}^\dagger b_{\mathbf{p}} . \end{aligned} \quad (52)$$

By discretizing to a single grid point with momentum $\mathbf{p} = 0$, we have

$$H_0 = H_{\text{Dirac}} + H_{\text{KG}} = M \sum_s (a^{s\dagger} a^s + c^{s\dagger} c^s) + m b^\dagger b . \quad (53)$$

By ignoring the spin degrees of freedom (spinless fermions), we find

$$H_0 = H_{\text{Dirac}} + H_{\text{KG}} = M(a^\dagger a + c^\dagger c) + m b^\dagger b . \quad (54)$$

A.2 Interaction Hamiltonian

In its most general form, the interaction Hamiltonian is given by [cf. Eq. (4) in Sec. 2.1 of the main text]

$$\begin{aligned} H_{\text{int}} &= \frac{g a_l^{3/2}}{2} \sum_{\mathbf{p}, \mathbf{p}'} \sum_{r,s} \left\{ \frac{1}{\sqrt{8\Omega_{\mathbf{p}}\Omega_{\mathbf{p}'}\omega_{\mathbf{p}-\mathbf{p}'}}} [a_{\mathbf{p}}^{r\dagger} \bar{u}^r(\mathbf{p}) + c_{-\mathbf{p}}^r \bar{v}^r(-\mathbf{p})] \right. \\ &\quad \times [a_{\mathbf{p}'}^s u^s(\mathbf{p}') + c_{-\mathbf{p}'}^{s\dagger} v^s(-\mathbf{p}')] (b_{\mathbf{p}-\mathbf{p}'} + b_{\mathbf{p}'-\mathbf{p}}^\dagger) + \text{H.c.} \Big\} . \end{aligned} \quad (55)$$

By restricting momentum space to a single site with $\mathbf{p} = 0$, we obtain

$$\begin{aligned} H_{\text{int}} &= \frac{g a_l^{3/2}}{2\sqrt{8M^2m}} \sum_{r,s} [(a^{r\dagger} \bar{v}^r + c^r \bar{u}^r) (a^s v^s + c^{s\dagger} u^s) (b + b^\dagger) + \text{H.c.}] \\ &= \frac{g a_l^{3/2}}{2\sqrt{8M^2m}} \sum_{r,s} [(a^{r\dagger} a^s \bar{u}^r u^s + a^{r\dagger} c^{s\dagger} \bar{u}^r v^s + c^r a^s \bar{v}^r u^s + c^r c^{s\dagger} \bar{v}^r v^s) \\ &\quad \times (b + b^\dagger) + \text{H.c.}] , \end{aligned} \quad (56)$$

where the momentum index/argument is dropped. For the spinor products in the non-relativistic limit we have

$$\begin{aligned}\bar{u}^r u^{s'} &= 2M\delta^{rs}, \\ \bar{u}^r v^{s'} &= 0, \\ \bar{v}^r u^{s'} &= 0, \\ \bar{v}^r v^{s'} &= -2M\delta^{rs}.\end{aligned}\tag{57}$$

By taking into account these last identities, the single-site Hamiltonian in Eq. (56) reduces to

$$\begin{aligned}H_{\text{int}} &= \frac{ga_l^{3/2}}{\sqrt{2m}} \sum_s (a^{s\dagger} a^s - c^s c^{s\dagger}) (b + b^\dagger) \\ &= \frac{ga_l^{3/2}}{\sqrt{2m}} \sum_s (a^{s\dagger} a^s + c^{s\dagger} c^s - 1) (b + b^\dagger).\end{aligned}\tag{58}$$

Finally, we ignore the spin degrees of freedom and restrict ourselves to the states with the vanishing total charge, which yields

$$H_{\text{int}} = \frac{ga_l^{3/2}}{\sqrt{2m}} (a^\dagger a + c^\dagger c - 1) (b + b^\dagger).\tag{59}$$

At this point we can express the lattice spacing a_l in terms of the boson mass via $a_l/(2m) = \beta\gamma$. Because β ought to be small for our single-site abstraction (the nonrelativistic limit), we use $\gamma \approx 1$. In this manner, we finally obtain the zero-dimensional interaction Hamiltonian

$$H_{\text{int}} = \frac{\eta}{2} (a^\dagger a + c^\dagger c - 1) (b + b^\dagger),\tag{60}$$

with $\eta \equiv 4mg\beta^{3/2}$ being the effective coupling strength.

B Boson mapping

The bosonic creation operator with a truncation at $\Lambda = 2^N - 1$ can be represented by the matrix

$$b_N^\dagger = \sum_{k=1}^{2^N-1} \sqrt{k} G_{N,k},\tag{61}$$

where $(G_{N,k})_{ij} = \delta_{i-1,k}\delta_{j,k}$. By defining $I_\pm = (I \pm Z)/2$ and $\sigma_\pm = (X \pm iY)/2$, we derive a recurrence relation for $G_{N,k}$ in terms of the qubit number N :

$$G_{N+1,k} = \begin{cases} I_+ \otimes G_{N,k} & \text{if } k \leq 2^N - 1, \\ \sigma_- \otimes \sigma_+^{\otimes N} & \text{if } k = 2^N, \\ I_- \otimes G_{N,k-2^N} & \text{if } k > 2^N. \end{cases}\tag{62}$$

By representing k as a bit string [cf. Eq. (15) in Sec. 3.3] we can straightforwardly find the explicit solution to Eq. (62):

$$G_{N,k} = \left(\frac{1}{2}\right)^N \bigotimes_{j=0}^{N-1} F_{j,k}.\tag{63}$$

The single-qubit operators $F_{j,k}$ depend on the binary string $q(k)$ as follows:

$$F_{j,k} = \begin{cases} I_j + Z_j & \text{if } q(k)_j = 0 \text{ and } \exists m < j : q(k)_m = 1, \\ I_j - Z_j & \text{if } q(k)_j = 1 \text{ and } \exists m < j : q(k)_m = 1, \\ X_j + iY_j & \text{if } q(k)_j = 0 \text{ and } \forall m < j : q(k)_m = 0, \\ X_j - iY_j & \text{if } q(k)_j = 1 \text{ and } \forall m < j : q(k)_m = 0, \end{cases} \quad (64)$$

which can be written more compactly as

$$F_{j,k} = \begin{cases} I_j + (-1)^{q_j(k)} Z_j & \text{if } \exists m < j : q(k)_m = 1, \\ X_j + (-1)^{q_j(k)} iY_j & \text{if } \forall m < j : q(k)_m = 0. \end{cases} \quad (65)$$

C Kraus-Cirac decomposition

In this section, we show how the unitary gate \mathcal{S} , defined in Eq. (29), is decomposed into a quantum circuit.

Every special unitary operation $U \in \text{SU}(4)$ can be written as

$$U = (K_4 \otimes K_3) N(\alpha, \beta, \gamma) (K_2 \otimes K_1), \quad (66)$$

where $K_1, K_2, K_3, K_4 \in \text{SU}(2)$ and

$$N(\alpha, \beta, \gamma) = \exp[i(\alpha XX + \beta YY + \gamma ZZ)], \quad (67)$$

with $\alpha, \beta, \gamma \in \mathbb{R}$. Assuming that \mathcal{S} takes the form from (66), we wish to find the single qubit gates K_j and the two-qubit rotation angles α, β, γ . We start by transforming \mathcal{S} to the magic basis. By making use of the magic gate

$$\mathcal{M} = \frac{1}{\sqrt{2}} \begin{pmatrix} 1 & i & 0 & 0 \\ 0 & 0 & i & 1 \\ 0 & 0 & i & -1 \\ 1 & -i & 0 & 0 \end{pmatrix}, \quad (68)$$

we find

$$\begin{aligned} V &= \mathcal{M}^\dagger \mathcal{S} \mathcal{M} \\ &= \frac{1}{4} \begin{pmatrix} -(\tilde{\lambda}_- + \tilde{\lambda}_+ - 2) & -i(\tilde{\lambda}_- - \tilde{\lambda}_+) & i(\tilde{\lambda}_- + \tilde{\lambda}_+ + 2) & \tilde{\lambda}_- - \tilde{\lambda}_+ \\ i(\tilde{\lambda}_- + \tilde{\lambda}_+ + 2) & -(\tilde{\lambda}_- - \tilde{\lambda}_+) & \tilde{\lambda}_- + \tilde{\lambda}_+ - 2 & -i(\tilde{\lambda}_- - \tilde{\lambda}_+) \\ -i(\tilde{\lambda}_- - \tilde{\lambda}_+) & -(\tilde{\lambda}_- + \tilde{\lambda}_+ - 2) & -(\tilde{\lambda}_- - \tilde{\lambda}_+) & -i(\tilde{\lambda}_- + \tilde{\lambda}_+ + 2) \\ -(\tilde{\lambda}_- - \tilde{\lambda}_+) & i(\tilde{\lambda}_- + \tilde{\lambda}_+ + 2) & i(\tilde{\lambda}_- - \tilde{\lambda}_+) & -(\tilde{\lambda}_- + \tilde{\lambda}_+ - 2) \end{pmatrix} \end{aligned} \quad (69)$$

The transformation to the magic basis has two beneficial properties. First, it diagonalizes $N(\alpha, \beta, \gamma) = \mathcal{M} D \mathcal{M}^\dagger$ such that

$$D = \text{diag} \left(e^{i(\alpha - \beta + \gamma)}, e^{-i(\alpha - \beta - \gamma)}, e^{i(\alpha + \beta - \gamma)}, e^{-i(\alpha + \beta + \gamma)} \right). \quad (70)$$

Second, the mapping $A \otimes B \rightarrow \mathcal{M}^\dagger (A \otimes B) \mathcal{M}$ precisely defines the isomorphism between the spaces $\text{SU}(2) \otimes \text{SU}(2)$ and $\text{SO}(4)$. Consequently, we may write $V = Q_1 D Q_2^T$, where the special orthogonal matrices $Q_1, Q_2 \in \text{SO}(4)$ and the

diagonal matrix D are obtained by performing a singular value decomposition. Here, we construct $V^T V = Q_2 D^2 Q_2^T$ with

$$V^T V = \frac{1}{2} \begin{pmatrix} -(a+b) & -i(a-b) & 0 & 0 \\ -i(a-b) & -(a+b) & 0 & 0 \\ 0 & 0 & -(a+b) & i(a-b) \\ 0 & 0 & i(a-b) & -(a+b) \end{pmatrix} \quad (71)$$

Through diagonalization (which can be performed block-wise here), we find

$$Q_2 = \frac{1}{\sqrt{2}} \begin{pmatrix} 0 & 0 & 1 & 1 \\ -1 & 1 & 0 & 0 \\ 0 & 0 & -1 & 1 \\ 1 & 1 & 0 & 0 \end{pmatrix}, \quad (72)$$

and

$$D = \text{diag} (e^{i\varphi}, e^{i\varphi}, e^{-i\varphi}, e^{-i\varphi}), \quad (73)$$

with $\varphi = \arctan[\sqrt{2}/(1 + \sqrt{3})]$, from which we conclude that $\alpha = \beta = 0$ and $\gamma = \varphi$. Q_1 is straightforwardly obtained through $Q_1 = V Q_2 D^{-1}$. At this point, we will spare the rest of the calculation, as it is only a matter of undoing the transformation to the magic basis.

D Generation of Pauli strings

In this appendix, we derive an algorithm to efficiently calculate the Pauli strings for a truncation using N qubits. Our approach is based on finding a recurrence relation between $b + b^\dagger$ truncated with N and $N + 1$ qubits [89]. Writing out $b + b^\dagger$ in the Fock state basis, we find:

$$\left(\begin{array}{cccc|cccc} 0 & \sqrt{1} & \cdots & 0 & 0 & & & \\ \sqrt{1} & 0 & \cdots & 0 & 0 & & & \\ \vdots & \vdots & \ddots & \vdots & \vdots & & & \\ 0 & 0 & \cdots & 0 & \sqrt{2^N - 1} & & & \\ 0 & 0 & \cdots & \sqrt{2^N - 1} & 0 & \sqrt{2^N} & & \\ \hline & & & & \sqrt{2^N} & 0 & \sqrt{2^N + 1} & \cdots \\ & & & & \sqrt{2^N + 1} & 0 & \cdots & 0 \\ & & & & \vdots & \vdots & \ddots & \vdots \\ & & & & 0 & 0 & \cdots & 0 \\ & & & & 0 & 0 & \cdots & \sqrt{2^{N+1} - 1} \\ & & & & & & & 0 \end{array} \right).$$

Note that the top left block is nothing but $(b + b^\dagger)_N$. In order to succinctly express the recurrence relation, we define $I_\pm = (I \pm Z)/2$ and $\sigma_\pm = (X \pm iY)/2$. The expression we find is given by

$$(b + b^\dagger)_{N+1} = (b + b^\dagger)_N \otimes I_+ + 2^N (\sigma_+^{\otimes N} \otimes \sigma_- + \sigma_-^{\otimes N} \otimes \sigma_+) + M_{\text{BR},N} \otimes I_-, \quad (74)$$

where $(b + b^\dagger)_1 = X$ and $M_{\text{BR},N}$ is the bottom right sub-matrix of the matrix above. The reason we do not write it out explicitly is that $M_{\text{BR},N}$ consists of the same Pauli strings as $(b + b^\dagger)_N$. Bearing this in mind, we write down the recurrence relation

$$S_{N+1} = S_N \otimes I \cup S_N \otimes Z \cup S(\sigma_+^{\otimes N} \otimes \sigma_- + \sigma_-^{\otimes N} \otimes \sigma_+), \quad (75)$$

for the set of Pauli strings S_N [cf. Eq. (38)], with $S_1 = \{X\}$.

Here, the Pauli operators I and Z come from the expansion of I_{\pm} . As discussed in Sec. 4.3, the set $S(\sigma_+^{\otimes N} \otimes \sigma_- + \sigma_-^{\otimes N} \otimes \sigma_+)$ consists of 2^N Pauli strings, which implies that the number of Pauli strings $|S_N|$ satisfies the difference equation

$$|S_{N+1}| = 2|S_N| + 2^N, \quad (76)$$

with $|S_1| = 1$. The explicit solution to this equation is given by

$$|S_N| = N 2^{N-1}. \quad (77)$$

E The distance metric

In this section, we derive the CNOT-cost of a time-step using the star+ancilla layout, depicted in Fig. 11(b). While the pure star layout from Fig. 11(a) makes use of a smaller number of CNOT gates, the ancilla qubit allows for easier gate cancellation in the transition zones, as no basis transformations are applied on the target qubit.

Let us consider the transition zone of two consecutive Pauli strings P_1 and P_2 . We will briefly describe the approach of Ref. [77] before introducing our improved cancellation technique. On indices where $P_1[i] = P_2[i]$, the CNOT gates cancel out. But for indices where $P_1[i] \neq P_2[i]$, one has to differentiate between two cases: (a) neither $P_1[i]$ nor $P_2[i]$ is I or (b) one of them is I . Case (a) requires two CNOTs, while (b) only needs one. Combining these results, the CNOT distance metric of Ref. [77] (cf. Eq. (15) in that reference) is defined as

$$|P_1 - P_2|_{\text{CNOT}} := \sum_{i \in [N]} 1_{P_1[i] \neq P_2[i]} (1 + 1_{I \notin \{P_1[i], P_2[i]\}}). \quad (78)$$

We will now modify this cost function by using circuit identities which reduce the CNOT-cost in case (a) to one. We start by considering transitions of the type $X \rightarrow Z$ or $Z \rightarrow X$, represented by the circuit in Fig. 25, which can be reduced to a single CNOT gate.

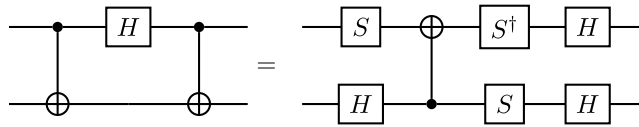


Figure 25: CNOT reduction in the $X \leftrightarrow Z$ transition circuit.

Next, we investigate the $Z \rightarrow Y$ and $Y \rightarrow Z$ transitions. Of course, $Y \rightarrow Z$ is just the inverse of $Z \rightarrow Y$ and can be obtained as the Hermitian conjugate. The circuit for $Z \rightarrow Y$ is shown in Fig. 26. In the first step, we used that S commutes with a control, and in the second one, we reuse the circuit from Fig. 25 for the $X \rightarrow Z$ transition.

It remains to simplify the circuit for $X \rightarrow Y$, depicted in Fig. 27. In the first step, we use that $HSH = S^\dagger HS^\dagger$ up to a global phase and the commutation of S^\dagger with the control. In the second step, we once again recycle the circuit for $X \rightarrow Z$ and undo the global phase.

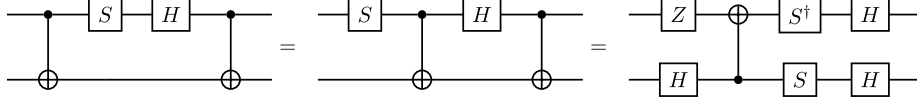


Figure 26: CNOT reduction in the $Z \rightarrow Y$ transition circuit.

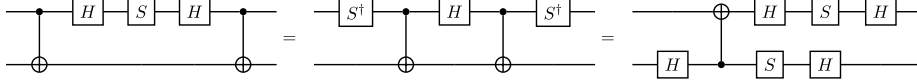


Figure 27: CNOT reduction in the $X \rightarrow Y$ transition circuit.

All these results together prove that any transition with $P_1[i] \neq P_2[i]$ can be implemented with only one CNOT gate, which implies that we have

$$|P_1 - P_2|_{\text{CNOT}} := \sum_{i \in [N]} 1_{P_1[i] \neq P_2[i]} = |P_1 - P_2|_{\text{Ham}}, \quad (79)$$

where $|P_1 - P_2|_{\text{Ham}}$ is the Hamming distance counting the number of disagreeing indices. Compared to the previous cost function in Eq. (78) this cuts the cost by up to 50%.

F Upper bound on the CNOT-cost

Using the recurrence formula for the Pauli strings (38) and the functions for the CNOT-cost of the start- and end layer as well as the transition zones, we will now derive an upper bound on the CNOT-cost of the circuit representing $\exp(-iH_b \Delta t)$ in first-order Trotterization. We first recall the recurrence formula for the Pauli strings [cf. Eq. (38)]

$$S_{N+1} = S_N \otimes I \cup S_N \otimes Z \cup S(\sigma_+^{\otimes N} \otimes \sigma_- + \sigma_-^{\otimes N} \otimes \sigma_+), \quad (80)$$

where $S_1 = \{X\}$.

In the following, $C(O)$ denotes the CNOT-cost of implementing the Pauli strings of the operator O in first-order Trotterization. Using the identities $C(S_N \otimes I) = C(S_N)$ and $C(S_N \otimes Z) = C(S_N) + 2$, as well as the fact that we can always cancel $2N$ CNOT-gates when transitioning from $S_N \otimes I$ to $S_N \otimes Z$, we find

$$C(S_N \otimes I \cup S_N \otimes Z) = 2C(S_N) + 2 - 2N. \quad (81)$$

For the second part, namely $S(\sigma_+^{\otimes N} \otimes \sigma_- + \sigma_-^{\otimes N} \otimes \sigma_+)$, we recall that this set contains all $(N+1)$ -digit Pauli strings made from X and Y with an even number of Y s. The start- and end layers of this set give us $2(N+1)$ CNOTs. To maximize the gate cancellation, we arrange the set using every other element of an $(N+1)$ -digit gray code. This way, only two characters change per transition. For $2^N - 1$ transition zones, we then find a total cost of $2^{N+1} - 2$. Combining these results, we arrive at the difference equation

$$C(S_{N+1}) \leq 2C(S_N) + 2^{N+1}, \quad (82)$$

with $C(S_1) = 2$. The explicit solution to this equation is given by

$$C(S_N) \leq N 2^N = 2|S_N|. \quad (83)$$

References

- [1] S. Lloyd, *Science* **273**, 1073 (1996).
- [2] C. Zalka, *Proc. R. Soc. London A* **454**, 313 (1998).
- [3] I. M. Georgescu, S. Ashhab, and F. Nori, *Rev. Mod. Phys.* **86**, 153 (2014).
- [4] For a recent review on superconducting qubits, see G. Wendin, *Rep. Prog. Phys.* **80**, 106001 (2017).
- [5] For a recent review of trapped-ion based platforms, see, e.g., C. D. Bruzewicz, J. Chiaverini, R. McConnell, and J. M. Sage, *Appl. Phys. Rev.* **6**, 021314 (2019).
- [6] For an up-to-date review of Rydberg-atom based platforms, see, e.g., M. Morgado and S. Whitlock, *AVS Quantum Sci.* **3**, 023501 (2021).
- [7] R. P. Feynman, *Int. J. Theor. Phys.* **21**, 467 (1982).
- [8] D. S. Abrams and S. Lloyd, *Phys. Rev. Lett.* **79**, 2586 (1997); *ibid.* **83**, 5162 (1999).
- [9] R. Somma, G. Ortiz, J. E. Gubernatis, E. Knill, and R. Laflamme, *Phys. Rev. A* **65**, 042323 (2002).
- [10] S. B. Bravyi and A. Y. Kitaev, *Ann. Phys. (N.Y.)* **298**, 10 (2002).
- [11] See, e.g., J. D. Whitfield, I. Biamonte, and A. Aspuru-Guzik, *Mol. Phys.* **109**, 735 (2011).
- [12] S. Raeisi, N. Wiebe, and B. C. Sanders, *New J. Phys.* **14**, 103017 (2012).
- [13] D. Wecker, M. B. Hastings, N. Wiebe, B. K. Clark, C. Nayak, and M. Troyer, *Phys. Rev. A* **92**, 062318 (2015).
- [14] R. Barends, L. Lamata, J. Kelly, L. García-Álvarez, A. G. Fowler, A. Megrant, E. Jeffrey, T. C. White, D. Sank, J. Y. Mutus, *et al*, *Nat. Commun.* **6**, 7654 (2015).
- [15] R. Babbush, N. Wiebe, J. McClean, J. McClain, H. Neven, and G. K. Chan, *Phys. Rev. X* **8**, 011044 (2018).
- [16] J.-M. Reiner, S. Zanker, I. Schwenk, J. Leppäkangas, F. Wilhelm-Mauch, G. Schön, and M. Marthaler, *Quantum Sci. Technol.* **3**, 045008 (2018).
- [17] Z. Jiang, K. J. Sung, K. Kechedzhi, V. N. Smelyanskiy, and S. Boixo, *Phys. Rev. Appl.* **9**, 044036 (2018).
- [18] For a recent review of applications in quantum chemistry, see, e.g., S. McArdle, S. Endo, A. Aspuru-Guzik, S. C. Benjamin, and X. Yuan, *Rev. Mod. Phys.* **92**, 015003 (2020).
- [19] A. Mezzacapo, J. Casanova, L. Lamata, and E. Solano, *Phys. Rev. Lett.* **109**, 200501 (2012).

- [20] A. Macridin, P. Spentzouris, J. Amundson, and R. Harnik, Phys. Rev. Lett. **121**, 110504 (2018).
- [21] A. Macridin, A. C. Y. Li, S. Mrenna, and P. Spentzouris, Phys. Rev. A **105**, 052405 (2022).
- [22] A. Miessen, P. J. Ollitrault, and I. Tavernelli, Phys. Rev. Res. **3**, 043212 (2021).
- [23] See, e.g., V. M. Stojanović, Phys. Rev. B **101**, 134301 (2020).
- [24] V. M. Stojanović, T. Shi, C. Bruder, and J. I. Cirac, Phys. Rev. Lett. **109**, 250501 (2012).
- [25] J. K. Nauth and V. M. Stojanović, Phys. Rev. B **107**, 174306 (2023).
- [26] F. Mei, V. M. Stojanović, I. Siddiqi, and L. Tian, Phys. Rev. B **88**, 224502 (2013).
- [27] V. M. Stojanović, M. Vanević, E. Demler, and L. Tian, Phys. Rev. B **89**, 144508 (2014).
- [28] V. M. Stojanović and I. Salom, Phys. Rev. B **99**, 134308 (2019).
- [29] V. M. Stojanović, Phys. Rev. Lett. **124**, 190504 (2020).
- [30] V. M. Stojanović, Phys. Rev. A **103**, 022410 (2021).
- [31] Y. Tong, V. V. Albert, J. R. McClean, J. Preskill, and Y. Su, Quantum **6**, 816 (2022).
- [32] E. A. Martinez, C. A. Muschik, P. Schindler, D. Nigg, A. Erhard, M. Heyl, P. Hauke, M. Dalmonte, T. Monz, P. Zoller, and R. Blatt, Nature (London) **534**, 516 (2016).
- [33] E. T. Holland, K. A. Wendt, K. Kravvaris, X. Wu, W. E. Ormand, J. L. DuBois, S. Quaglioni, and F. Pederiva, Phys. Rev. A **101**, 062307 (2020).
- [34] M. J. Cervia, A. B. Balantekin, S. N. Coppersmith, C. W. Johnson, Peter J. Love, C. Poole, K. Robbins, and M. Saffman, Phys. Rev. C **104**, 024305 (2021).
- [35] M. Kreshchuk, W. M. Kirby, G. Goldstein, H. Beauchemin, and P. J. Love, Phys. Rev. A **105**, 032418 (2022).
- [36] N. H. Nguyen, M. C. Tran, Y. Zhu, A. M. Green, C. H. Alderete, Z. Davoudi, and N. M. Linke, PRX Quantum **3**, 020324 (2022).
- [37] N. Kico, A. Roggero, and M. J. Savage, Rep. Prog. Phys. **85**, 064301 (2022).
- [38] M. Heyl, Rep. Prog. Phys. **81**, 054001 (2018).
- [39] M. E. Peskin and D. V. Schroeder, *An Introduction To Quantum Field Theory* (Avalon Publishing, 1995).
- [40] H. Yukawa, Proc. Phys. Math. Soc. Jpn. (3rd Series) **17**, 48 (1935).

- [41] J. Preskill, *Quantum* **2**, 79 (2018).
- [42] IBM Quantum, <https://quantum-computing.ibm.com/>
- [43] A. Peres, *Phys. Rev. A* **32**, 3266 (1985).
- [44] M. Born and V. Fock, *Z. Physik* **51**, 165 (1928)
- [45] T. Albash and D. A. Lidar, *Rev. Mod. Phys.* **90**, 015002 (2018)
- [46] V. M. Stojanović and J. K. Nauth, *Phys. Rev. A* **106**, 052613 (2022).
- [47] V. M. Stojanović and J. K. Nauth, arXiv:2302.12483.
- [48] E. Kökcü, D. Camps, L. Bassman, J. K. Freericks, W. A. de Jong, R. Van Beeumen, and A. F. Kemper, *Phys. Rev. A* **105**, 032420 (2022).
- [49] B. Peng, S. Gulania, Y. Alexeev, and N. Govind, *Phys. Rev. A* **106**, 012412 (2022).
- [50] M. Suzuki, *Commun. Math. Phys.* **51**, 183 (1976).
- [51] N. Hatano and M. Suzuki, in *Quantum annealing and other optimization methods* (Springer, Berlin, 2005), pp. 37-68.
- [52] V. V. Shende, I. L. Markov, and S. S. Bullock, *Phys. Rev. A* **69**, 062321 (2004).
- [53] V. M. Stojanović, *Phys. Rev. A* **99**, 012345 (2019).
- [54] For an introduction, see, e.g., S. S. Skiena, *The Algorithm Design Manual* (Springer-Verlag, London, 2012), Second Edition.
- [55] R. Bellman, *J. Assoc. Comput. Mach.* **9**, 61 (1962).
- [56] M. Held and R. M. Karp, *J. Soc. Indust. Appl. Math.* **10**, 196 (1962).
- [57] N. Christofides, *Worst-case analysis of a new heuristic for the traveling salesman problem*, Technical report, Graduate School of Industrial Administration, Carnegie-Mellon University, Pittsburgh (PA), 1976.
- [58] Qiskit Runtime, <https://github.com/Qiskit/qiskit-ibm-runtime/>
- [59] J. Ranninger, J. M. Robin, and M. Eschrig, *Phys. Rev. Lett.* **74**, 4027 (1995).
- [60] S. P. Jordan, K. S. M. Lee and J. Preskill, *Quant. Inf. Comput.* **14**, 1014 (2014).
- [61] A. Ciavarella, *Phys. Rev. D* **102**, 094505 (2020).
- [62] R. C. Farrell, I. A. Chernyshev, S. J. M. Powell, N. A. Zemlevskiy, M. Illa, and M. J. Savage, *Phys. Rev. D* **107**, 054513 (2023).
- [63] H. F. Trotter, *Proc. Am. Math. Soc.* **10**, 545 (1959).
- [64] M. A. Nielsen and I. L. Chuang, *Quantum Computation and Quantum Information* (Cambridge University Press, Cambridge, 2000).

- [65] P. Jordan and E. Wigner, Z. Phys. **47**, 631 (1928).
- [66] J. T. Seeley, M. J. Richard, and P. J. Love, J. Chem. Phys. **137**, 224109 (2012).
- [67] B. Terhal and D. P. DiVincenzo, Phys. Rev. A **65**, 032325 (2002).
- [68] B. Kraus and J. I. Cirac, Phys. Rev. A **63**, 062309 (2001).
- [69] F. Vatan and C. Williams, Phys. Rev. A **69**, 032315 (2004).
- [70] D. Gross, Y.-K. Liu, S. T. Flammia, S. Becker, and J. Eisert, Phys. Rev. Lett. **105**, 150401 (2010).
- [71] D. Gross, IEEE Trans. Inf. Theory **57**, 1548 (2011).
- [72] J. B. Altepeter, D. F. James, and P. G. Kwiat, in *Quantum State Estimation*, Lecture Notes in Physics, Edited by M. Paris and J. Řeháček (Springer, Berlin Heidelberg, 2004), vol. 649, pp. 113-145.
- [73] A. W. R. Smith, J. Gray, and M. S. Kim, PRX Quantum **2**, 020348 (2021).
- [74] J. A. Smolin, J. M. Gambetta, and G. Smith, Phys. Rev. Lett. **108**, 070502 (2012).
- [75] Qiskit Experiments, <https://github.com/Qiskit/qiskit-experiments>
- [76] A. Uhlmann, Rep. Math. Phys. **9**, 273 (1976).
- [77] K. Gui, T. Tomesh, P. Gokhale, Y. Shi, F. T. Chong, M. Martonosi, and M. Suchara, arXiv:2001.05983.
- [78] See, e.g., Quantinuum, System Model H1 Product Data Sheet, Version 5.00 (2022).
- [79] G. Magnifico, T. Felser, P. Silvi, and S. Montangero, Nat. Commun. **12**, 1 (2021).
- [80] O. Kern, G. Alber, and D. L. Shepelyansky, Eur. Phys. J. D **32**, 153 (2005).
- [81] O. Kern and G. Alber, Phys. Rev. Lett. **95**, 250501 (2005).
- [82] K. Temme, S. Bravyi, and J. M. Gambetta, Phys. Rev. Lett. **119**, 180509 (2017).
- [83] Y. Li and S. C. Benjamin, Phys. Rev. X **7**, 6 (2017).
- [84] S. McArdle, X. Yuan, and S. Benjamin, Phys. Rev. Lett. **122**, 180501 (2019).
- [85] P. Czarnik, A. Arrasmith, P. J. Coles, and L. Cincio, Quantum **5**, 592 (2021).
- [86] Y. Guo and S. Yang, PRX Quantum **3**, 040313 (2022).
- [87] For a review, see T. Giurgica-Tiron, Y. Hindy, R. LaRose, A. Mari, and W. J. Zeng, 2020 IEEE International Conference on Quantum Computing and Engineering (QCE), Denver, CO, USA, 2020.

- [88] M. Geller, Z. Holmes, P. J. Coles, and A. Sornborger, Phys. Rev. Research **3**, 033200 (2021).
- [89] X.-Y. Huang, L. Yu, X. Lu, Y. Yang, D.-S. Li, C.-W. Wu, W. Wu, and P.-X. Chen, arXiv:2105.12563.